





RESEARCH ARTICLE | MARCH 03 2025

# The impact of platform motion on the aerodynamic characteristics of floating offshore wind turbine arrays

Xiang Li (李翔) ; Qing Xiao (肖清)  ; Yang Huang (黄扬) 

 Check for updates

*Physics of Fluids* 37, 037102 (2025)

<https://doi.org/10.1063/5.0256441>



## Articles You May Be Interested In

KoopmanLab: Machine learning for solving complex physics equations

*APL Mach. Learn.* (September 2023)

Experimental realization of a quantum classification: Bell state measurement via machine learning

*APL Mach. Learn.* (September 2023)

03 March 2025 16:56:54



**Physics of Fluids**  
Special Topics  
Open for Submissions

[Learn More](#)



# The impact of platform motion on the aerodynamic characteristics of floating offshore wind turbine arrays

Cite as: Phys. Fluids **37**, 037102 (2025); doi: 10.1063/5.0256441

Submitted: 4 January 2025 · Accepted: 3 February 2025 ·

Published Online: 3 March 2025






View Online



Export Citation



CrossMark

Xiang Li (李翔),  Qing Xiao (肖清),  <sup>a)</sup> and Yang Huang (黄扬) 

## AFFILIATIONS

Department of Naval Architecture, Ocean and Marine Engineering, University of Strathclyde, Glasgow G4 0LZ, United Kingdom

Note: This paper is part of the Special Topic, Wave-Structure Interaction.

<sup>a)</sup> Author to whom correspondence should be addressed: [qing.xiao@strath.ac.uk](mailto:qing.xiao@strath.ac.uk)

## ABSTRACT

Floating offshore wind turbines (FOWTs) are gaining increasing attention within the industry. In this paper, the impact of platform motion on the aerodynamic characteristics of the FOWT array is numerically investigated. A high-fidelity numerical tool with the Computational Fluid Dynamics (CFD) method is further developed based on the open-source CFD toolbox OpenFOAM by coupling the Actuator Line Model. Three turbines with different arrangements based on tandem and staggered layouts are simulated. Significant wake interactions are observed by investigating the flow field around the downstream region, the velocity and turbulence variation due to the wake interaction has been studied. The capacity factor of the total system of a tandem layout is 50% in the most common scenarios, while it is 92% for the staggered layouts. The motion of the turbine, due to the floating platform, has a minor influence on the time-averaged power output but significantly influences the power fluctuation. In gridded layouts, the downstream FOWT can have up to 25% higher fluctuation amplitude than fixed one, while for staggered layouts, this can reach 80% in the most critical case. The flow field also indicates that strong wind turbulence reduces the impact of platform motion on power fluctuations, especially for the third turbine, with the most significant wake interaction. By analyzing the power output and the platform motion, it is found that the pitch and surge motion of the OC4 platform have an opposite influence on the power output. Thus, a coupled model considering both degrees of freedom is necessary.

© 2025 Author(s). All article content, except where otherwise noted, is licensed under a Creative Commons Attribution (CC BY) license (<https://creativecommons.org/licenses/by/4.0/>). <https://doi.org/10.1063/5.0256441>

## I. INTRODUCTION

To address the energy crisis and promote environmentally friendly energy sources, wind turbines have been extensively developed and deployed all over the world. Offshore areas, with their favorable wind conditions, are increasingly becoming the preferred locations for these installations. As the distance from the shore increases and water depths exceed 50 meters, fixed foundations become impractical due to their high costs. Consequently, floating offshore wind turbines (FOWTs) have gained prominence in recent years as a more viable solution.

Wake interactions is crucial for overall wind farm efficiency, occurring when the disrupted, slower, and more turbulent airflow behind a turbine impacts downstream turbines, reducing their efficiency and increasing mechanical stress. Although extensive research exists about onshore turbines and the resulting wake interactions,<sup>1–5</sup> the non-stationary attribute of the FOWT brings in unique issues than

onshore ones. For example, the floating platform's motion significantly affects FOWT's performance compared to fixed turbines.<sup>6</sup> Although the motion's effect is subtle when the motion is small, a large oscillation was found for the power output with a larger motion.<sup>7,8</sup> Such fluctuation also reflects on the trust of the turbines, which may lead to fatigue issues and affect their durability. This periodic motion also leads to a periodic wake variation, and faster wake recovery for the floating scenario, thus may improve the performance of the affected downstream turbines.<sup>9</sup> It is also observed for FOWTs that the mean power output of FOWTs is higher than that of fixed turbines, though the difference is very slight.<sup>10</sup> The aerodynamics also influence platform motion in turn, as the thrust and moment from the upper turbine cause a drift in surge motion and a change in mean pitch.<sup>11</sup> These differences introduce new avenues of research for FOWTs.

The wake interaction between multiple floating turbines also exhibits unique features compared to fixed-bottom turbines. The

upstream platform's motion alters its wake characteristics, which changes the inflow condition for the downstream turbine and the resulting aerodynamic performance. For the tandem FOWTs, the platform surge motion of the upstream turbine impacts the downstream turbine and showed that surge motion slightly increases the average power of both turbines and enhances flow mixing in the wake.<sup>12</sup> In the tandem FOWTs study where the downstream turbine is fixed, the fluctuation matching the wave period was also observed in the downstream turbine's power output, indicating that the platform motion leads to a periodic velocity change in the wake,<sup>13–15</sup> and impacting the downstream turbine. In addition, the aerodynamic properties, such as the amplitude of power output and thrust, are found to be sensitive to motion phases of the two FOWTs. For the downstream turbine, a significant amplitude of power output increase was observed when the motion phase lag between the turbines was not aligned, highlighting the importance of synchronized turbine motion on the wake interaction. In addition, changing the position of the downstream turbine along the cross-flow direction leads to a significant increase in its load and power efficiency, with a maximum of 41% increase among the studied cases.<sup>16</sup>

However, the mentioned studies are based on two FOWTs, which are not enough to account for the wake interactions between FOWTs as well as their dynamic response. In an operating onshore wind farm, one turbine might be affected by more than one turbine ahead of it along the wind direction.<sup>17</sup> Other scenarios may also lead to such multiple-wake interaction, for example, the change in wind direction<sup>18</sup> and the nacelle yaw offset.<sup>19,20</sup> Nevertheless, in floating scenarios, it remains unclear how the platform motion impacts the aerodynamic characteristics of FOWTs with multiple wakes interactions. In this case, the inflow condition for FOWTs becomes more complicated and affects the periodic motion response. The change in motion mode, in turn, affects the aerodynamic characteristics.

On the multiple wake interaction of FOWTs, there's limited research, which may be caused by many reasons. Because such studies require more than three FOWTs, experiments are infeasible due to space limitations and cost. For numerical studies, there also limited options due to the absence of study tools capable of incorporating non-stationary wind turbines.<sup>21</sup> Studies on single FOWT has been conducted using OpenFAST which is designed to simulate FOWTs<sup>22</sup> or reduced-order method like Free Vortex Methods.<sup>23,24</sup> For wake-interaction study, Computational Fluid Dynamics (CFD) method is commonly used for fixed turbines, which has also been modified for FOWT studies. A blade-resolved CFD method was used to study the OC4 platform with NREL 5 MW turbine, considering both aerodynamics and hydrodynamics.<sup>11</sup> However, for multiple turbine studies, it becomes infeasible due to extremely large computational costs. Thus, a CFD study with Actuator Disk Model (ADM) is conducted, where there's no need for the meshing the blade geometry, and the platform motion is simplified as prescribed surge motion of the turbines.<sup>12</sup> It is found the motion-wake interaction are not clearly reflected in the downstream turbines. With more accurate Actuator Line Model (ALM) instead of ADM,<sup>13–15</sup> the motion-wake interaction was found has a significant influence on the downstream turbines. A two-FOWT array is simulated using the ALM method coupled with the hydrodynamic model and aerodynamic model, which can both consider the platform's motion and its influences on the wake.<sup>25</sup> It was also found that platform motion heightens turbulence in the wake area, which

speeds up the recovery of wake velocity and leads to a broader wake. For studies with more than two FOWTs, limited CFD research can be found to the authors' knowledge only with reduced-order methods, mostly the wake-model-based methods. Kheirabadi and Nagamune developed a low-fidelity dynamic wind farm model for FOWT farm simulation.<sup>26</sup> Three FOWTs are studied with a distance of  $7D$ . Dynamic phenomena in floating wind farms, including the movement of wakes, the variability of wind speed and direction, and the motion of floating platforms, can be seen and are consistent with logical, physical understanding and intuition. For this kind of low-fidelity model, the resolution and the difficulty of incorporating the hydrodynamic model limit their application.

In this paper, the interaction between platform motion and the multiple wake effects has been studied. Since simulating the entire FOWT farm is infeasible due to computational limits, an array consisting of three FOWTs with varying arrangements is studied. This is the minimum number of turbines required to investigate multiple wake interactions. To deal with this problem, an integrated numerical modeling tool is developed by incorporating ALM into the current CFD tool, together with the mooring model. For each layout, the dynamic response of each FOWT is analyzed and the aerodynamic characteristics of the FOWT farms are compared. The platform motion effect on the aerodynamics is also studied.

## II. METHODOLOGY

The FSI problem of the FOWT is simulated using an integrated CFD toolbox based on OpenFOAM code.<sup>27</sup> The hydrodynamic forces are computed by integrating the pressure field around the platform surface obtained from solving the Navier-Stokes equations, while the aerodynamic forces from the turbine are resolved simultaneously via the Actuator Line Model. These combined forces and moments are fed into the six-degrees-of-freedom (6DoF) motion equations to compute the platform's dynamic response.

In this model, the flow is governed by incompressible Navier-Stokes (NS) equations. Since moving mesh is utilized, the Arbitrary Lagrangian-Eulerian (ALE) form of NS equations is adopted

$$\frac{\partial u_i}{\partial x_i} = 0, \quad (1)$$

$$\frac{\partial \rho u_i}{\partial t} + \frac{\partial}{\partial x_j} (\rho u_i (u_j - \hat{u}_j)) = -\frac{\partial p}{\partial x_i} + \frac{\partial}{\partial x_j} \left[ \mu_{\text{eff}} \left( \frac{\partial u_i}{\partial x_j} + \frac{\partial u_j}{\partial x_i} \right) \right] + \rho g_i + f_{\sigma i} + f_{e i}, \quad (2)$$

where  $x_i$  is the Cartesian coordinate, the subscript  $i$  represents the  $i$ th component. The index  $i = 1, 2, 3$  denote the  $x, y,$  and  $z$  directions, respectively.  $u_i$  and  $\hat{u}_i$  denote the speed of the fluid and the moving mesh, respectively.  $t$  is the time,  $\rho$  is the fluid density, and  $p$  is the dynamic pressure.  $\mu_{\text{eff}} = \rho(\nu + \nu_t)$  denotes the effective dynamic viscosity of the fluid, in which  $\nu$  and  $\nu_t$  are the kinematic and eddy viscosity, respectively.  $g_i$  is the gravity acceleration,  $f_{\sigma i}$  is the surface tension and  $f_{e i}$  is the body force from the wind turbine. To accurately solve the vortex and forces on the turbines and platforms, the Large Eddy Simulation (LES) wall-adapted local eddy-viscosity (WALE) model is used in this study.

### A. Hydrodynamics solving

The free-surface between air and water are handled by Volume of Fluid (VOF) method.<sup>28</sup> The volume fraction  $\alpha$  for each cell is defined to govern the interface of air and water, which represents the percentage of the cell occupied by the water.  $\alpha = 1$  means the whole cell is occupied by water, while  $\alpha = 0$  it is filled with air. A value between 1 and 0 means that the cell is located at the free surface. The following transport equations govern the volume fraction:

$$\frac{\partial \alpha}{\partial t} + \frac{\partial}{\partial x_j} ((u_i - \hat{u}_i)\alpha) + \frac{\partial}{\partial x_j} (u_{ri}(1 - \alpha)\alpha) = 0. \quad (3)$$

To maintain a sharp interface and ensure that the  $\alpha$  remains conservative and bounded between 0 and 1, an artificial compression term  $\nabla \cdot (u_r(1 - \alpha)\alpha)$ , where  $u_r$  is a velocity field used to compress the interface and only functions near the free surface.

To generate numerical waves, the fluid velocity at the inlet boundary is prescribed using Stokes second-order wave theory<sup>29</sup>

$$u = \frac{\pi H}{T} \frac{\cosh k(z+d)}{\sinh kd} \cos \theta + \frac{3\pi H}{4T} \left(\frac{\pi H}{L}\right) \frac{\cosh 2k(z+d)}{\sinh^4 kd} \cos 2\theta, \quad (4)$$

$$w = \frac{\pi H}{T} \frac{\sinh k(z+d)}{\sinh kd} \sin \theta + \frac{3\pi H}{4T} \left(\frac{\pi H}{L}\right) \frac{\sinh 2k(z+d)}{\sinh^4 kd} \sin 2\theta, \quad (5)$$

where  $H$  and  $T$  denote the wave height and wave period,  $k$  and  $d$  denote wave number and water depth, and  $\theta$  is the phase.

To impose non-reflection boundary conditions on the computational outlet boundary, an active wave-absorbing scheme is utilized which can significantly reduce the computational domain size required by the relaxation zone.<sup>29</sup> The corrected velocity at the outlet boundary is described by

$$\Delta u = -\Delta \eta \frac{\pi H}{T} \frac{\cosh k(z+d)}{\sinh kd}, \quad (6)$$

where  $\Delta \eta$  is the difference of the surface elevation  $\eta$  due to reflected waves.

### B. Aerodynamics solving

To calculate the forces and power output of the wind turbines, as well as the interaction with the surrounding flow field, the ALM, as a high-fidelity aerodynamic modeling approach, is used in this CFD solver. The turbine blades are first discretized into a series of spanwise line segments or actuator lines, as shown in Fig. 1. These lines represent the blade's center of pressure or a specified percentage of the chord from the leading edge, typically at 25%.

Then for each line segment, the local flow conditions, including the angle of attack  $\alpha$  and local relative wind speed  $\mathbf{U}_{rel}$ , are needed for the force calculation. These are determined by the interaction of the incident wind with the rotational motion of the rotor and any additional motions of the turbine platform, for example, the wave-induced motion for a FOWT. The relative velocity can be expressed as follows:

$$\mathbf{U}_{rel} = \mathbf{U}_{in} + \mathbf{U}_R + \mathbf{U}_M = \mathbf{U}_{in} + \boldsymbol{\Omega} \times \mathbf{r} + \mathbf{U}_M, \quad (7)$$

where  $\mathbf{U}_{in}$  is the velocity of the incoming wind velocity in the blade-aligned coordinate system,  $\mathbf{U}_R$  is the velocity induced by rotor's

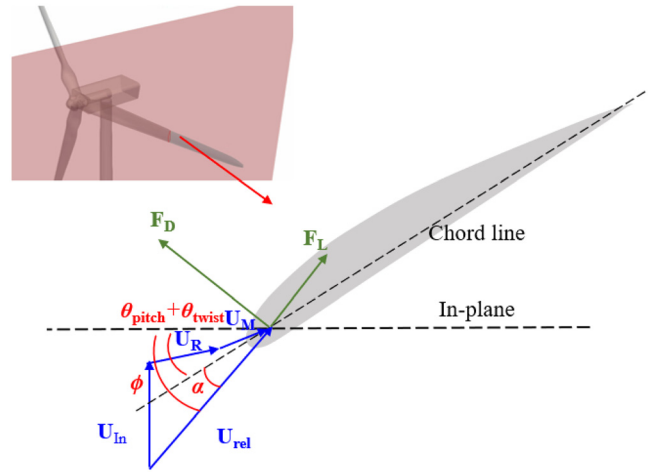


FIG. 1. Sketch of the velocity components at the blade section.

rotation,  $\boldsymbol{\Omega}$  is the rotor's angular velocity,  $\mathbf{r}$  is the vector that extends from the blade root to the concerned actuator point, and  $\mathbf{U}_M$  is the platform-induced velocity.  $\mathbf{U}_M$  is translated to the motion of blades since the influence of  $\mathbf{U}_M$  on aerodynamic performance is significant. The translated position  $\mathbf{X}_M$  and velocity  $\mathbf{U}_M$  of specific actuator point are

$$\mathbf{X}_M = \boldsymbol{\eta}_1 + \boldsymbol{\eta}_2(\mathbf{x}_j - \mathbf{x}_c), \quad (8)$$

$$\mathbf{U}_M = \dot{\boldsymbol{\eta}}_1 + \dot{\boldsymbol{\eta}}_2(\mathbf{x}_j - \mathbf{x}_c), \quad (9)$$

where  $\mathbf{x}_j$  is the points' position without considering the platform's motion, and  $\mathbf{x}_c$  is the initial platform's center of rotation.  $\boldsymbol{\eta}_1$  and  $\boldsymbol{\eta}_2$  are the displacement and rotation of the platform, respectively.

Based on the obtained local flow conditions, the aerodynamic forces are computed using airfoil data. These forces are broken down into lift and drag components per segment and are functions of the local angle of attack, the relative wind speed, and the chord length of the blade segment. This force can be determined by the following equation:

$$\mathbf{f} = (F_L, F_D) = 0.5\rho|\mathbf{U}_{rel}|^2 c(c_l \mathbf{e}_l + c_d \mathbf{e}_d), \quad (10)$$

where  $F_L$  and  $F_D$  are lift and drag forces, respectively.  $\mathbf{e}_l$  and  $\mathbf{e}_d$  are the unit vectors of lift and drag forces, respectively.  $c_l$  and  $c_d$  are the lift and drag coefficients, respectively.  $\rho$  is the air density, and  $c$  is the chord length. These coefficients can be found in the airfoil data as given properties for specific turbines.

When calculating the aerodynamic loads on wind turbine blades using blade element theory, it's crucial to account for the effects of vortex shedding from both the blade tip and root. These effects lead to modifications in the aerodynamic load predictions, necessitating the application of specific correction factors. The tip and root loss factor,  $F_{tip}$  and  $F_{root}$  are introduced to adjust for the reduced aerodynamic efficiency in these areas due to the vortex shedding

$$F_{tip} = \frac{2}{\pi} \cos^{-1} e^{-\frac{N_b R_{rotor} - r}{2 r \sin \phi}}, \quad F_{root} = \frac{2}{\pi} \cos^{-1} e^{-\frac{N_b r - R_{hub}}{2 r \sin \phi}}, \quad (11)$$

where  $R_{rotor}$  and  $R_{hub}$  are the radius of the rotor and hub, respectively, and  $N_b$  is the number of blades. The corrected loads on the turbines  $f$  are then corrected by

$$f' = f \cdot F_{tip} \cdot F_{root}. \tag{12}$$

By integrating the loads along the blade’s spanwise direction, the power output  $P$  and thrust  $F_T$  can be calculated. The calculated forces are then projected onto the flow field using a body force projection. This step ensures the forces are smoothly distributed over the CFD mesh, preventing numerical instabilities. To project the body forces, a regularization kernel function  $\eta$  is used

$$\eta(d_j) = \frac{1}{\varepsilon^3 \pi^{\frac{3}{2}}} \exp\left[-\left(\frac{d_j}{\varepsilon}\right)^2\right], \tag{13}$$

where  $d_j$  is the distance between the grid node and the actuator point. The constant parameter  $\varepsilon$  decides the width of the projection region and has significant effects on the computation results and is recommended to set it to twice the minimum mesh size to ensure a stable numerical solution.<sup>30</sup> It can be seen that this function only influences the cells near the element. The force projected to the cells is then calculated by

$$f_e(x, y, z, t) = \sum_{j=1}^{N_p} f(x_j, y_j, z_j, t) \eta_e(d_j). \tag{14}$$

After the force projection, the modified flow field equations, now including the body forces from the actuator lines, are solved using CFD techniques to capture the resulting flow field, like the velocity and the pressure, which is used for the aerodynamic force’s calculation.

### III. VALIDATION AND VERIFICATION

Validation has been conducted to confirm the accuracy of the present tool. The accuracy of ALM has been validated for fixed turbines, as shown in [Appendixes A and B](#). To validate the ALM in scenarios with floating turbines, a simulation has been conducted in which the upstream turbine was subjected to a prescribed surge motion while the downstream turbine remained fixed. The specifications for both turbines were based on the NREL 5 MW blades shown in [Table I](#), with a given TSR of 7.0 for the upstream turbine and 9.62 for the downstream turbine. They were spaced at a distance of  $3D$ , as shown in [Fig. 2](#).

Three different scenarios were tested, each characterized by a unique surge motion for the upstream turbine shown in [Eq. \(15\)](#)

$$x = A_s \sin\left(\frac{2\pi}{T_s} t\right), \tag{15}$$

where  $A_s$  is the amplitude of the prescribed surge motion.  $A_s = 1.02$  m in case 1, 2.04 m in case 2, and 3.06 m in case 3.  $T_s$  is the surge period, which remains  $T_s = 9$  s in all three cases. Each case aimed to discern how varying surge amplitudes impact the performance metrics of the turbines. The mesh setup follows the same rule as the fixed ones in [Appendix B](#). The boundary condition can be seen in [Fig. 2](#), where the bottom boundary is set to a non-slip boundary. The uniform wind velocity is set above the free surface at the inlet boundary. The results are compared with the CFD simulation results by [Arabgolarcheh et al.](#)<sup>15</sup>

[Figure 3](#) presents the normalized power coefficients, by the averaged power, for the upstream and downstream turbines. For the upstream turbine, a close examination reveals that the temporal evolution of  $C_p$  for all three cases exhibits a periodic fluctuation with the

TABLE I. Properties of the FOWT.

Wind turbine properties	
Wind regime	IEC Class 1 A
Rotor orientation	Upwind
Number of blades	3
Rotor diameter	126 m
Hub diameter and height	3 and 90 m
Cut-in/out wind speed	4/25 m/s
Rated wind speed	11.4 m/s
Rated rotor speed	5.0 MW
Rated power	90 m/s
Gross properties	
Total mass	$1.414 \times 10^7$ kg
Pitch inertia about center of mass	$1.315 \times 10^{10}$ kg m <sup>2</sup>
Yaw inertia about center of mass	$1.906 \times 10^{10}$ kg m <sup>2</sup>
Roll inertia about center of mass	$1.315 \times 10^{10}$ kg m <sup>2</sup>
Displacement	$1.399 \times 10^4$ m <sup>3</sup>
Mooring parameters	
Number of mooring lines	3
Angle between adjacent lines	120°
Radius to anchors from center of rotation	837.6 m
Mooring line diameter	0.0766 m
Unit mass	113.35 kg/m
Unit mass under water	108.63 kg/m

same period as  $T_s$ . Unlike fixed cases, this fluctuation is significant, and the amplitude increases with the motion amplitude and reaches 0.4 of the time-averaged power output with  $A_s = 3.06$  m. For the downstream turbine, although it is fixed, the power output also has a periodic variation with the same period, although with a much smaller amplitude than the upstream turbine. This indicates the influence of the upstream turbine on the performance of the downstream turbine, which arises from the periodic wake fluctuations caused by the upstream turbines’ platform motion. Results of both turbines show good agreement with the reference, showing the accuracy of the present method. [Figure 4](#) illustrates the normalized thrust coefficient  $C_t$ , which also shows a similar trend and agrees well with the referenced data.

### IV. RESULTS AND DISCUSSION

This study employs regular wave conditions as an input to systematically investigate the fundamental coupling mechanisms between sea conditions and the FOWT array. The controlled wave environment enables effective decoupling of the targeted interaction effects from confounding factors associated with irregular wave spectra and stochastic sea states. Different cases are studied, which can be categorized into two main layouts: gridded layouts and staggered layouts.

#### A. Parameters for numerical simulation

The setup of the computational domain of the numerical simulation is shown in [Fig. 5](#). The platform is composed of three offset

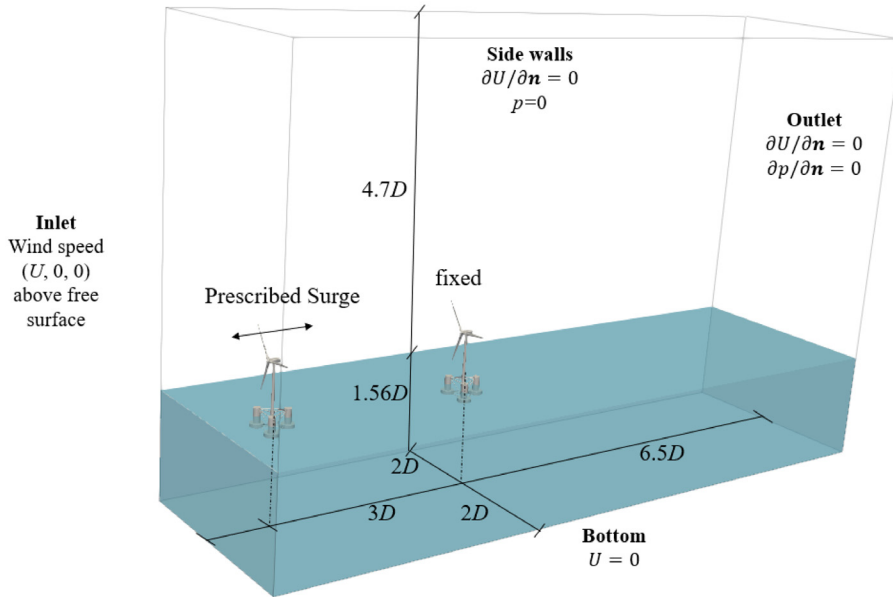


FIG 2. Sketch of the computational domain with tandem turbines.

columns and one center column, which are connected by crossbars. To reduce the complexity and computational time, the crossbars are omitted in this simulation, which has been proved to have little influence on the results.<sup>31</sup> The dimension of the computational domain is  $11D \times 6D \times 6.27D$  and the distance between each turbine along the  $x$  direction is  $3D$ . Although much larger distance is usually adopted in real scenarios, the primary focus of this study is to investigate the aerodynamic interactions and wake interference between turbines. A  $3D$  spacing better captures the main characteristics of wake interactions and turbine performance changes due to interference.

The boundary conditions are set as follows. At the upper part of the inlet boundary, which is above the static water level, a constant wind velocity  $U$  along the  $x$  axis is applied, which is a rated speed of  $11.4$  m/s. While variations in wind speed and direction, such as yawed

conditions or gusts, could influence the results, these factors are beyond the current scope and will be addressed in future studies.

For the lower part, a prescribed wave generation velocity is applied. At the side walls and the upper part of the outlet boundary, the Neumann boundary condition is assumed for both velocity and pressure. The lower part of the outlet boundary is set as an active wave-absorbing boundary. The bottom boundary is set to a non-slip boundary.

The computational mesh is shown in Fig. 6. To guarantee the accuracy of the simulation and to maintain an acceptable computational time, different levels of refinement are applied. The CFD mesh cells near the free surface are refined along the  $z$  direction, keeping the cell length along the  $z$  direction is  $1/8$  of the wave height. The mesh is also refined near the platforms' surface to accurately capture the hydrodynamics force. To capture the wake interaction, the wake zone

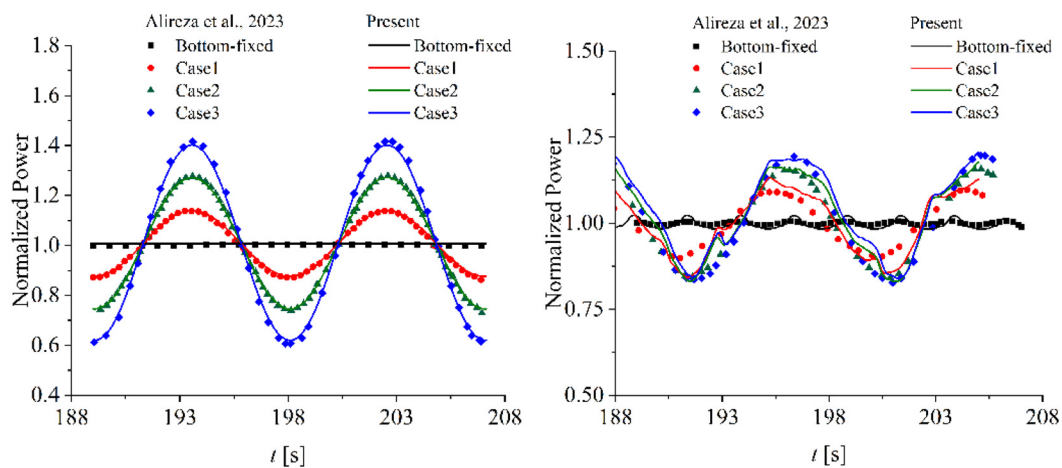


FIG. 3. Normalized  $C_p$  coefficients for the (a) upstream turbine (b) downstream turbine for cases 1–3 within two prescribed motion cycles.

03 March 2025 16:56:54

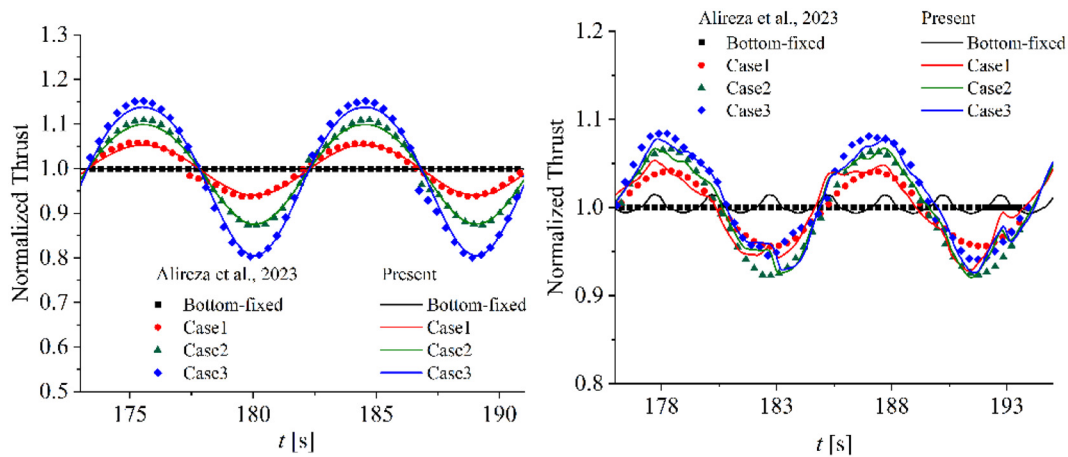


FIG. 4. Normalized  $C_t$  coefficients for the (a) upstream turbine (b) downstream turbine for cases 1–3 within two prescribed motion cycles.

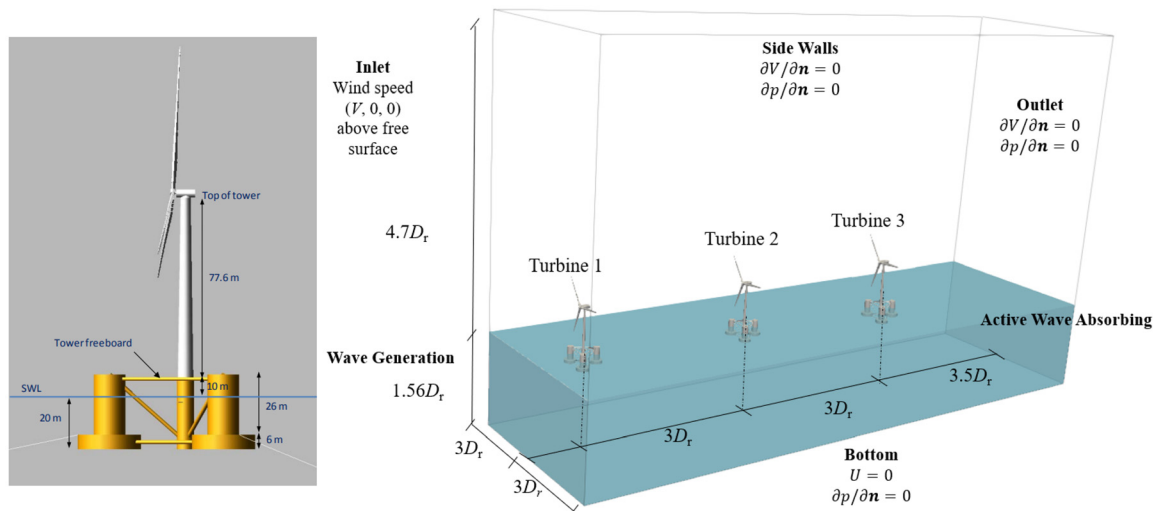


FIG. 5. Sketch of (a) the DeepCwind FOWT system and (b) the computational domain with three turbines with in-line arrangement for case 1.

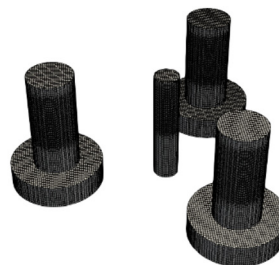
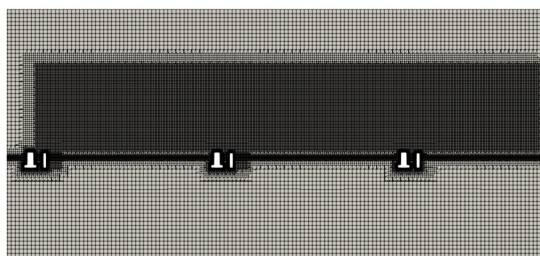


FIG. 6. Mesh of the domain and the platform.

behind the first turbine is refined with a mesh cell length of 2 m in the wind direction. This cell size has been proven to be adequate for ALM simulation of the NREL.<sup>25</sup>

The PIMPLE algorithm is used to solve the pressure–velocity coupling. A second-order Crank–Nicolson scheme is used for

temporal discretization. A second-order upwind scheme is adopted for convective terms. Gradient terms are handled via a second-order cell-limited Gauss linear scheme.

To study the wake interaction within a wind farm for different scenarios, three turbines with different arrangements are studied,

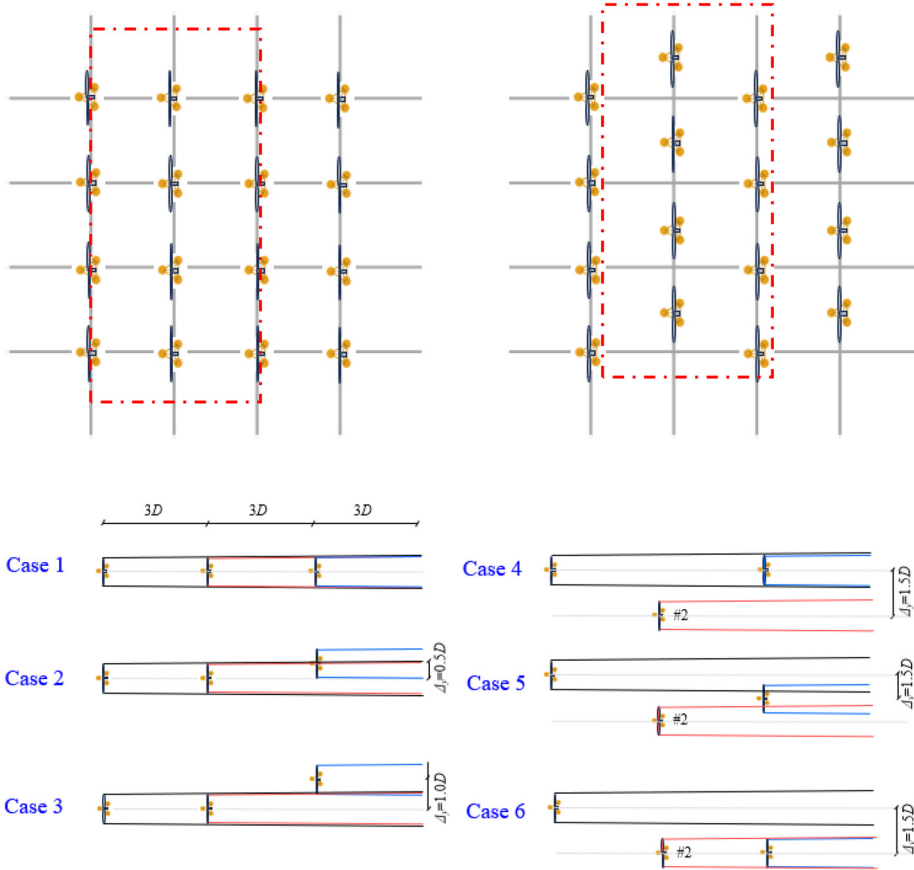


FIG. 7. Sketch of gridded and staggered layout in a wind farm.

FIG. 8. Position of the FOWT and its wake zone. The black, red, and blue lines represent the wake zones of turbines 1, 2, and 3, respectively.

which are derived from the gridded and staggered layouts. The scenarios of these derived layouts may come from the optimization of basic layouts and possess irregular features,<sup>32</sup> or the position change due to the platform motion. For these novel layouts, the mechanism of the multiple wake interaction would be complicated and important.<sup>33–37</sup> The first and second FOWTs are deployed either in a gridded layout (cases 1–3) or a staggered layout (cases 4–6), both are commonly used layouts for wind farms, as in Fig. 7, which present totally different wake interaction features. Thus, both layouts are simulated in this study. The position of the third turbine varies within the wake region of the other two turbines, which is shown in Fig. 8 and Table II. The spacing between each turbine along the x axis,  $\Delta x$  is fixed as  $3D$  for all cases, which is the same as that in the validation part for comparison.<sup>15,38,39</sup> The main difference between these cases is their spacing along the y axis  $\Delta y$ , where the subscripts in  $\Delta y_{12}$  mean the spacing between the second and first turbine. In order to decouple and analyze the contribution of platform motion, six special cases 1<sub>b</sub>–6<sub>b</sub> are studies where the third turbine is set to be fixed.

**B. Mesh and time-step dependence test**

To investigate the impact of mesh resolution and time step sensitivity, various configurations involving different mesh sizes and time steps were implemented. The tandem layout used in case 1 is chosen, and the three turbines are set to be fixed. Three different meshes are chosen for

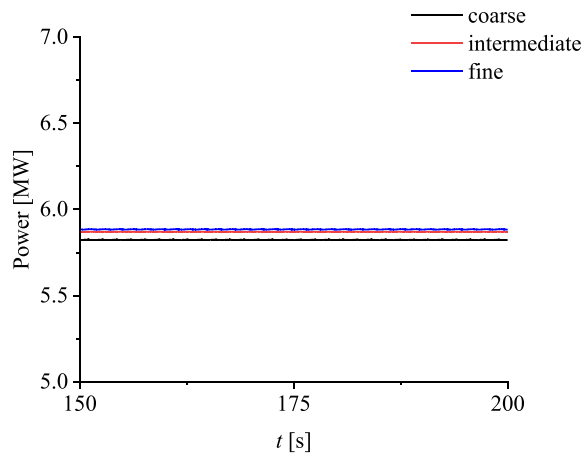
the mesh sensitivity analysis. The mesh configurations vary by the length of the cell for the mesh within the wake region: 1.5 m for the coarse mesh, 2.0 m for the intermediate mesh, and 2.5 m for the fine mesh.

As shown in Fig. 9(a), for the first and second turbines, compared to the fine and intermediate mesh, the power output of the coarse mesh is lower, while the results of the former two have basically

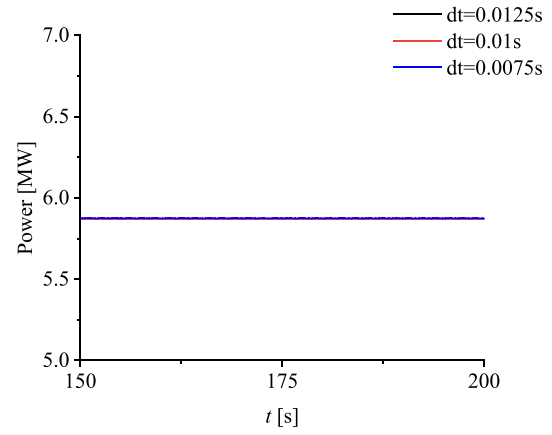
TABLE II. Different layouts of the FOWTs.

	$\Delta y_{12}$	$\Delta y_{13}$	3rd FOWT condition
Gridded layout	Case 1	0	Floating
	Case 1b		Fixed
	Case 2	0	Floating
	Case 2b	0.5D	Fixed
	Case 3	0	Floating
	Case 3b	1.0D	Fixed
Staggered layout	Case 4	1.5D	Floating
	Case 4b		Fixed
	Case 5	1.5D	Floating
	Case 5b	0.75D	Fixed
	Case 6	1.5D	Floating
	Case 6b	1.5D	Fixed

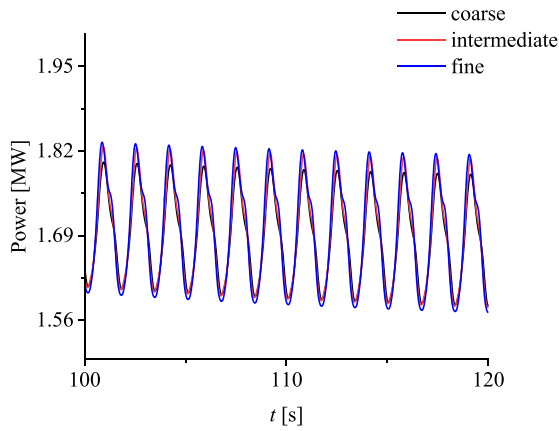




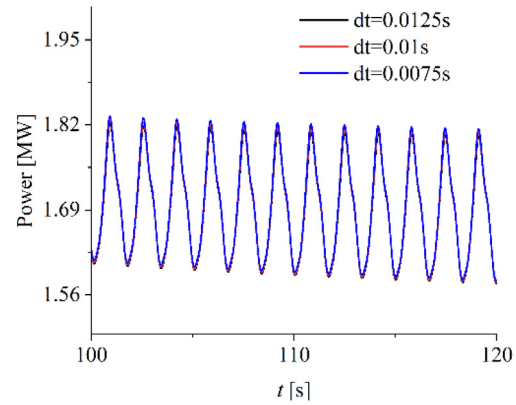
(a) Turbine 1



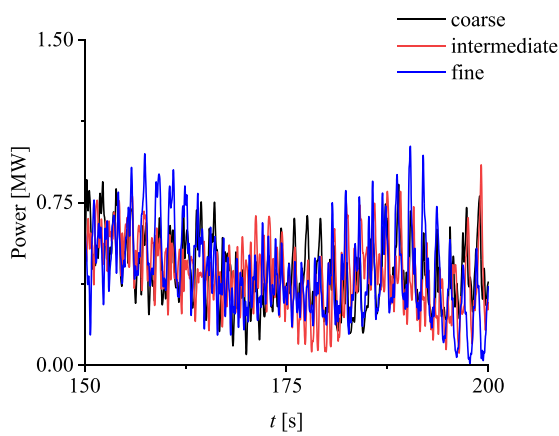
(b) Turbine 1



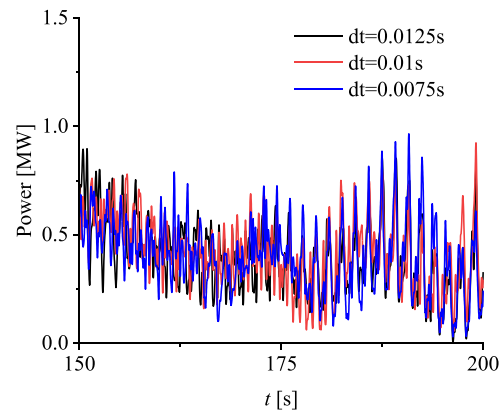
(c) Turbine 2



(d) Turbine 3



(e) Turbine 2



(f) Turbine 3

**FIG. 9.** Time history of the power output of three turbines. (a), (c) and (e) are the results for three turbines with different mesh resolutions. (b), (d) and (f) are the results for three turbines with different time steps.

converged. For the third turbine, the differences between the three results are significant. Since the wake is complicated and fully turbulent, it is hard to get the absolute converged results, but the amplitude and averaged value is similar. To balance the time cost and accuracy of the simulation, the intermediate mesh is chosen for the following research. For the time step dependency test, three time steps of 0.0125, 0.01, and 0.0075 s were examined. Similar to the mesh convergence test, the results converge after using smaller time steps for the two upstream turbines. Although the gap for the third turbine is observed, the results can still be accepted. Consequently, a time step of 0.01 s is chosen. The total cell of the simulation is around nine million, with a slight variance depending on the specific layouts. The computations are made in parallel with 5 nodes (180 cores) for each case using Cirrus UK National Tier-2 HPC Service, each compute node contain two 2.1 GHz, 18-core Intel Xeon E5-2695 (Broadwell) series processors. Each of the cores in these processors support 2 hardware threads (hyperthreads). The typical simulation time for one case is around 3–4 wave periods per day, which may vary depending on the specific cases. For example, for case 1, the total computational cost is 3.5 days with simulation time of 20 wave periods.

**C. Gridded layouts**

To analyze the FOWTs in gridded layouts, this section is divided into three subsections. Section IV C 1 covers the hydrodynamics of the

FOWTs, focusing on the motion response of FOWTs in the array. Section IV C 2 examines the aerodynamic performance of the wind farm and the wake interactions among the FOWTs. Since the above two aspects are correlated, Sec. IV C 3 investigates the influence of the platform motion on aerodynamics and wake characteristics. To achieve this goal, cases 1<sub>b</sub> to 3<sub>b</sub> are conducted, where the third turbine is set as fixed. By comparing them with the floating cases, the effect of platform motion is isolated.

**1. Hydrodynamics of FOWTs**

Among cases 1–3, the first and second turbines are in tandem arrangement. For the third turbine, different offsets from the x axis  $\Delta y_{13}$  are selected, with  $\Delta y_{13}$  ranging from 0 to  $D$ , as indicated in Table II.

Figure 10 shows the dynamic response of each FOWT, which is deeply related to the wake interaction in two aspects. First, the motion of each FOWT in a given case differs due to wake interaction between upstream and downstream turbines. Second, the position of the third FOWT varies in cases 1–3, which also affects the wake interaction. For the first aspect, take case 1 as an example, the first upstream turbine experiences uniform wind conditions and exhibits the largest surge and pitch motion. The second turbine, located in the wake of the first one, displays a decreased motion amplitude. Meanwhile, the third turbine decreases its motion further, influenced by the complex turbulent

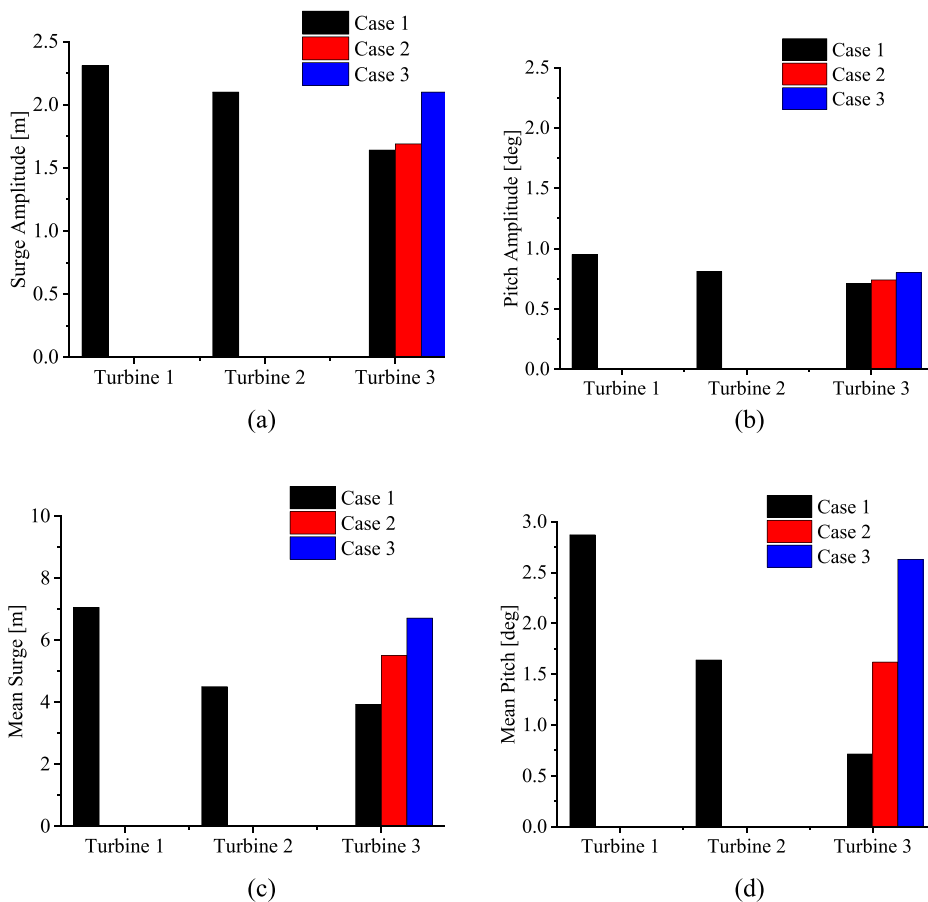


FIG. 10. (a) Surge and (b) pitch motion amplitude, time-averaged (c) surge and (d) pitch of different FOWTs.

03 March 2025 16:56:54

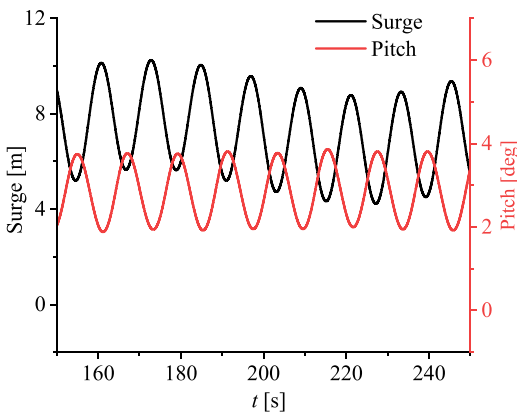


FIG. 11. Surge and pitch time series of the third turbine in case 1.

wake of the above two upstream turbines. The primary reason for the sequentially decreased motion is that the velocity deficit in the downstream wakes decreases the thrust of downstream turbines, thus lowering the load on the platforms in both surge and pitch directions. This will be further addressed in Sec. IV C 2 where the aerodynamics analysis will be focused. For the second aspect, as the offset  $\Delta y_{13}$  increases from cases 1 to 3, the third turbine shifts further from the wake zone of the upstream turbines, resulting in a significant increase in the mean surge and pitch in Figs. 10(c) and 10(d), where the mean pitch of the third turbine is 3.6 times greater than in case 1, almost approaching the level of the first upstream turbine. This is because the swept area of the wind turbines is less influenced by the low-speed zone in the wake from cases 1 to 2. The motion amplitude is also seen to be increased in Figs. 10(a) and 10(b). When the third turbine is fully within the wake zone of the two upstream turbines, the turbulent wake with higher frequencies interferes with the turbine's periodic motion. The resulting irregular loads result in more complex dynamic responses, causing the turbine to experience a broader range of motion frequencies and amplitudes, further diminishing the dominance of its primary periodic motion. However, when the turbine moves out of the

wake zone, this interference decreases, and the amplitude of its motion response increases. This will also be confirmed in Sec. IV C 2.

Another finding is that the surge and pitch motion are opposite in phase for present cases, as indicated by Fig. 11, where the time-dependent surge and pitch motion are shown. This implies that for the present combination of turbine and floating platform, the relative wind velocity variation caused by pitch and surge are coupled and opposite, which is also confirmed in other OC4 platform studies.<sup>11,40</sup> In other words, the pitch motion compensates for the relative wind speed caused by the surge motion. Therefore, instead of studying a single degree of freedom of platform, a coupled simulation that considers multiple degrees of freedom is necessary for accurate results.

### 2. Aerodynamics and wake interaction of FOWTs

The time-mean power output of the third turbine shown in Fig. 12 indicates that the two upstream turbines remain unaffected by the existence of the third turbine. Hence, the power output of the first and second turbines remains constant across cases 1–3. When  $\Delta y_{13} = 0$  in case 1, the third turbine is aligned with the two upstream turbines, having a minimum power output among the three turbines of about 1 MW. With  $\Delta y_{13}$  increasing from 0 to  $D$ , the power output increases significantly to around 4.8 MW but still less than the first turbine, which means the wake interaction still affects the turbines' efficiency. This significant increase shows the turbine position has a profound effect on its power output.

Another key element of aerodynamic performance is the fluctuation of the power output, which can be induced by both the wake interaction and the motion of the platform. The amplitude of the power output, estimated by its standard deviation multiplied by  $\sqrt{2}$ , indicates it gets smaller with the increase in  $\Delta y_{13}$  in Fig. 12. For the first turbine, the amplitude is mainly caused by the periodic motion of the platform induced by waves, reaching a maximum of 0.75 MW. However, for the second and third turbines, they are under the combined influence of the unsteady varied wake and the periodic platform motion, the amplitude gradually decreases as reflected in Fig. 12(a). The dominant factor varies depending on the case, which will be further explained in detail in Sec. IV C 3.

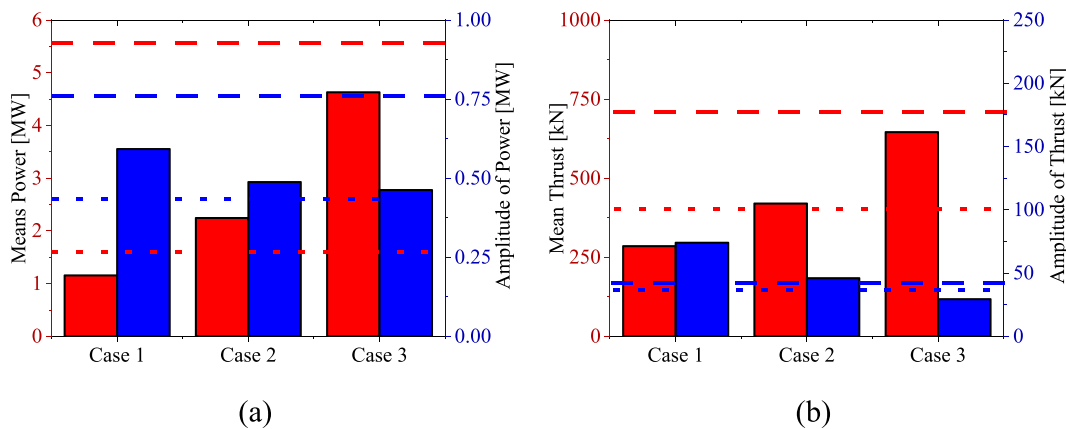


FIG. 12. (a) Time-averaged power output and amplitude of the power and (b) time-averaged thrust and amplitude of the thrust of the third turbine. The dashed lines denote the physical quantities of the first FOWT, while the dotted lines denote the physical quantities of the second FOWT.

The thrust of the third turbine is summarized in Fig. 12, shows a similar trend to the power output. Among different FOWTs in case 1, the thrust decreases sequentially from turbine 1 to 3, which confirms the hypothesis in Sec. IV C 1 and Fig. 10 that the progressive wake decreases the thrust of downstream turbines and leads to a smaller motion response.

The flow field characteristics directly affect the performance of the turbines. For example, time-averaged velocity influences the mean power output. Turbulence intensity  $I$ , a dimensionless measure of the strength of velocity fluctuations relative to the mean flow velocity, is related to power fluctuation.

$$I = \text{std}(u)/U, \quad (16)$$

where  $u$  is the transient wind speed. To observe their effects on the aerodynamic performance, the velocity field at a specific time instant  $t = 200$  s is shown in Fig. 13 at the hub height. From Fig. 13(a<sub>1</sub>), a distinct low-speed wake region can be observed behind the first turbine and an even lower speed zone can be found behind the second turbine, which causes the power reduction for the downstream turbines, as confirmed in Fig. 12. As the third turbine gradually repositions along the  $y$ -axis from Figs. 13(a<sub>1</sub>)–13(c<sub>1</sub>) and moves out of the wake area, the inflow conditions improve, resulting in a recovery of its power output. This velocity recovery is evident from Figs. 13(a<sub>2</sub>)–13(c<sub>2</sub>), where the time-averaged velocity distribution behind the first turbine exhibits a bell-shaped form, which is essentially symmetrical. Behind the second turbine, a more noticeable velocity deficit can be found, and the maximum velocity reduction occurs at the axial position and gradually decreases along the  $y$ -direction. For the third turbine, the velocity deficit affects it most in case 1, and the influence of this wake decreases as the position offset  $\Delta y$  increases, leading to a gradual increase in power.

From Figs. 13(a<sub>3</sub>)–13(c<sub>3</sub>), the turbulence intensity can be analyzed. Behind the first turbine, the increase in turbulence intensity is not significant. Therefore, the power fluctuation of the second turbine is not greatly affected by the turbulence intensity but is primarily dominated by the platform motion. When the two wakes interact and propagate to the third turbine, the air from the center and edges of the rotor plane is thoroughly mixed, maximizing turbulence intensity. At this point, the turbine's power fluctuation is more influenced by the turbulence of the wind field rather than platform motion. This will be further demonstrated in Sec. IV C 3.

The vortex structures shown in Fig. 14 is presented by the Q-criterion, which is colored by the velocity. The free surface is also shown with its color denoting the surface elevation. For case 1 in Fig. 14(a), the vortices can be seen symmetrically shed from the tip of the 1st wind turbine's blades and grow progressively larger with increasing distance. 3D helical wakes form downstream of the trailing edge, with the spacing between the generated vortex rings increasing with propagation distance, which might be caused by the velocity recovery along the propagating path: the velocity recovers gradually with larger spacing, allowing the rings to move at a higher speed, increasing the intervals. As these vortices pass the 2nd turbine, they mix with the vortices generated by it, creating complex turbulence and reducing the power output of the subsequent 3rd turbine.

In addition to the tip vortex shedding, a stable wake band is also formed near the root of the first turbine's blades. There is minimal interaction between this wake and the tip-generated wake behind the first turbine. Along the turbine axis, the vortices show a symmetric

distribution of positive and negative values. After passing the second turbine, they break down into upper and lower regions of small positive and negative vortices, respectively, and then completely mix after the third turbine. The well-defined rings generated by the blade tips are replaced by a chaotic, turbulent area.

As the third turbine is progressively re-positioned further in the  $y$ -direction, from Figs. 14(b)–14(c), its right side encounters an area of non-turbulent flow. Additionally, well-defined vortices gradually form behind the right-side tip and root of the blades. This leads to an incremental increase in aerodynamic power, as shown in Fig. 12, where its aerodynamic power is restored to 87% of that of the first turbine by shifting the third turbine out by one rotor diameter.

### 3. Platform motion contribution to aerodynamics performance

To better understand what exactly the impact of the motion of platform on the wind turbine aerodynamic features is, in this section, we study several sceneries where the platform's motion is eliminated for the third turbine, i.e., cases 1b to 3b.

The impact of platform motion on the power output can be intuitively observed in the time series of the power output in Fig. 15. The power output of the first turbine is smooth and sinusoidal, possessing the same period as the incident waves. For the second turbine, the power output decreases, and some high-frequency fluctuations appear on the basis of the sinusoidal power curve. Nevertheless, this curve also features a regular periodic variation, which means the power variation of the second turbine is still governed by the platform's sinusoidal motion, which is well reflected from Fig. 13 that the turbulence intensity for the second turbine is not significant and has a minor effect on it. For the 3<sup>rd</sup> turbine, which is located further downstream, these high-frequency disruptions become more pronounced, indicating a substantial impact from the wake effect. The FFT analysis in Fig. 15 illustrates that from the first turbine to the third turbine, there is a decline in the energy correlating with the wave frequency, while the energy associated with the blade-passing frequency exhibits an uptick. Furthermore, harmonic frequencies, which are multiples of the fundamental frequency, can also be found for downstream turbines implying the downstream turbines are more influenced by wind turbulence rather than waves. This effect is especially apparent for turbine 3, which is influenced by both turbines 1 and 2.

The time series of the third FOWT is presented for different cases in Fig. 16, including comparisons with the fixed cases. Both floating and fixed turbines appear the same motion period. The frequency components can be found in the FFT analysis shown in Fig. 16(a). Given case 1<sub>b</sub> with a  $\Delta y_{13} = 0$ , the stationary turbine exhibits a peak at the wave frequency of 0.083 Hz. This peak results from the periodic wake oscillations induced by the upstream FOWTs. In the floating scenario, this peak is more substantial; the difference between them represents the contribution from the motion of the third FOWT. With the increasing of  $\Delta y_{13}$  in cases 2b and 3b, the turbine moves further away from the wake zone of the upstream turbines. Consequently, the component of energy at the wave frequency becomes less pronounced.

The influence of the FOWT's motion response on the aerodynamic performance is shown in Fig. 17. The results are presented as the percentage difference between the floating and fixed cases relative to the fixed cases. It can be observed that whether the third FOWT is fixed or not only has minimal effect on the time-averaged power

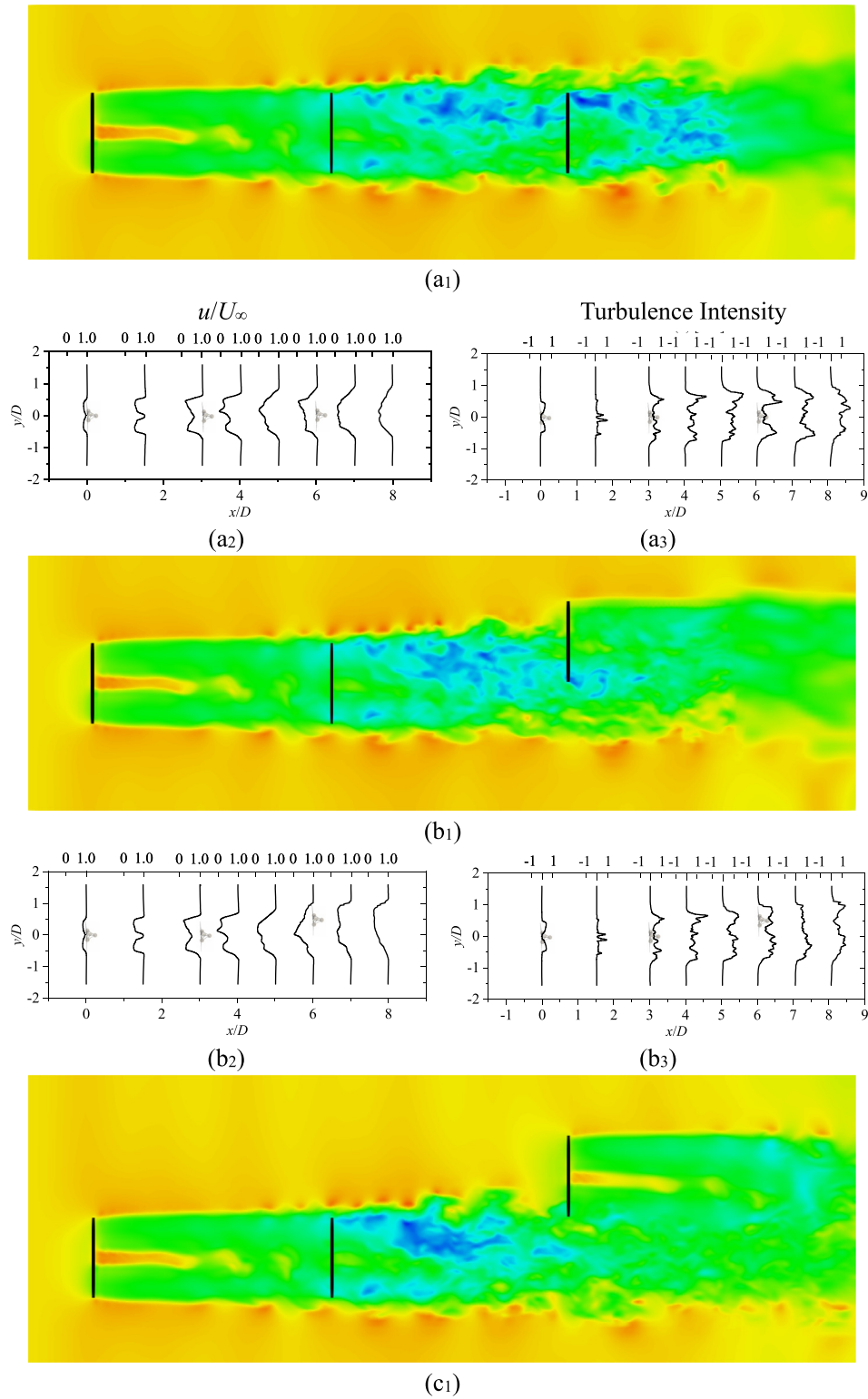


**FIG. 13.** (a<sub>1</sub>–c<sub>1</sub>) Contours of spanwise velocity at hub height for  $t = 200$  s; (a<sub>2</sub>–c<sub>2</sub>) the time-averaged velocity profile  $\bar{u}/U$  at different cross sections in the horizontal plane at hub height. (a<sub>3</sub>–c<sub>3</sub>) The corresponding time-averaged turbulence intensity profile. The subscripts denote the case number.

03 March 2025 16:56:54

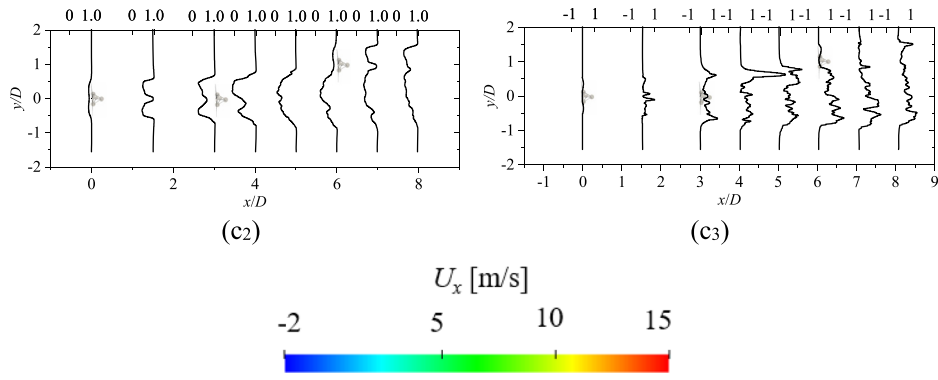


FIG. 13. (Continued.)

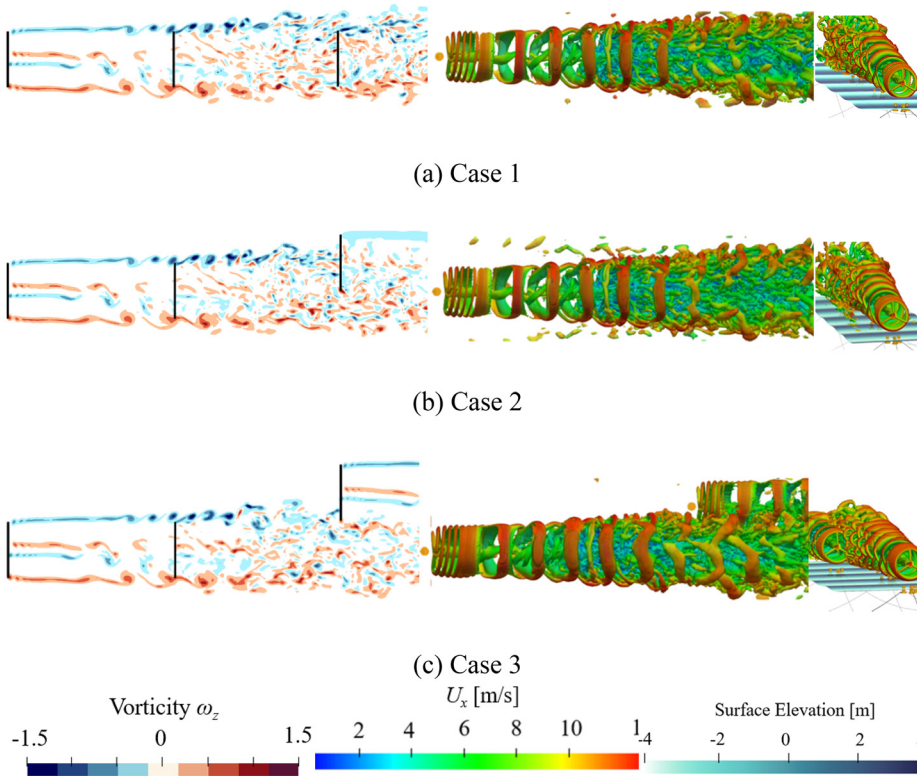


FIG. 14. Contours of spanwise vorticity at hub height and the vortex evolution (top and side view) represented by iso-surface of  $q=0.002$  at  $t=200$  s of each case. The surface elevation is also presented.

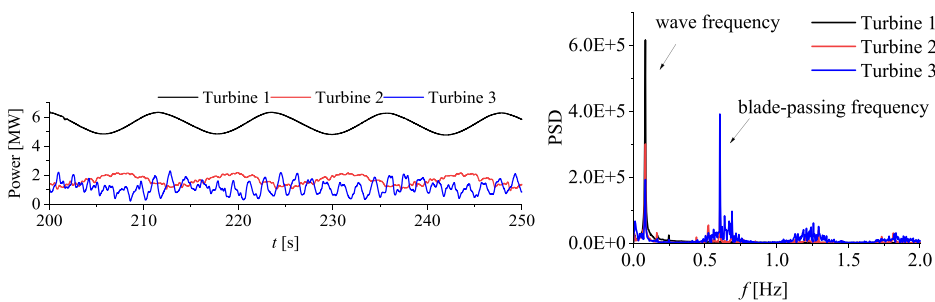


FIG. 15. Time series and FFT analysis of the power output of three turbines in case 1.

03 March 2025 16:56:54

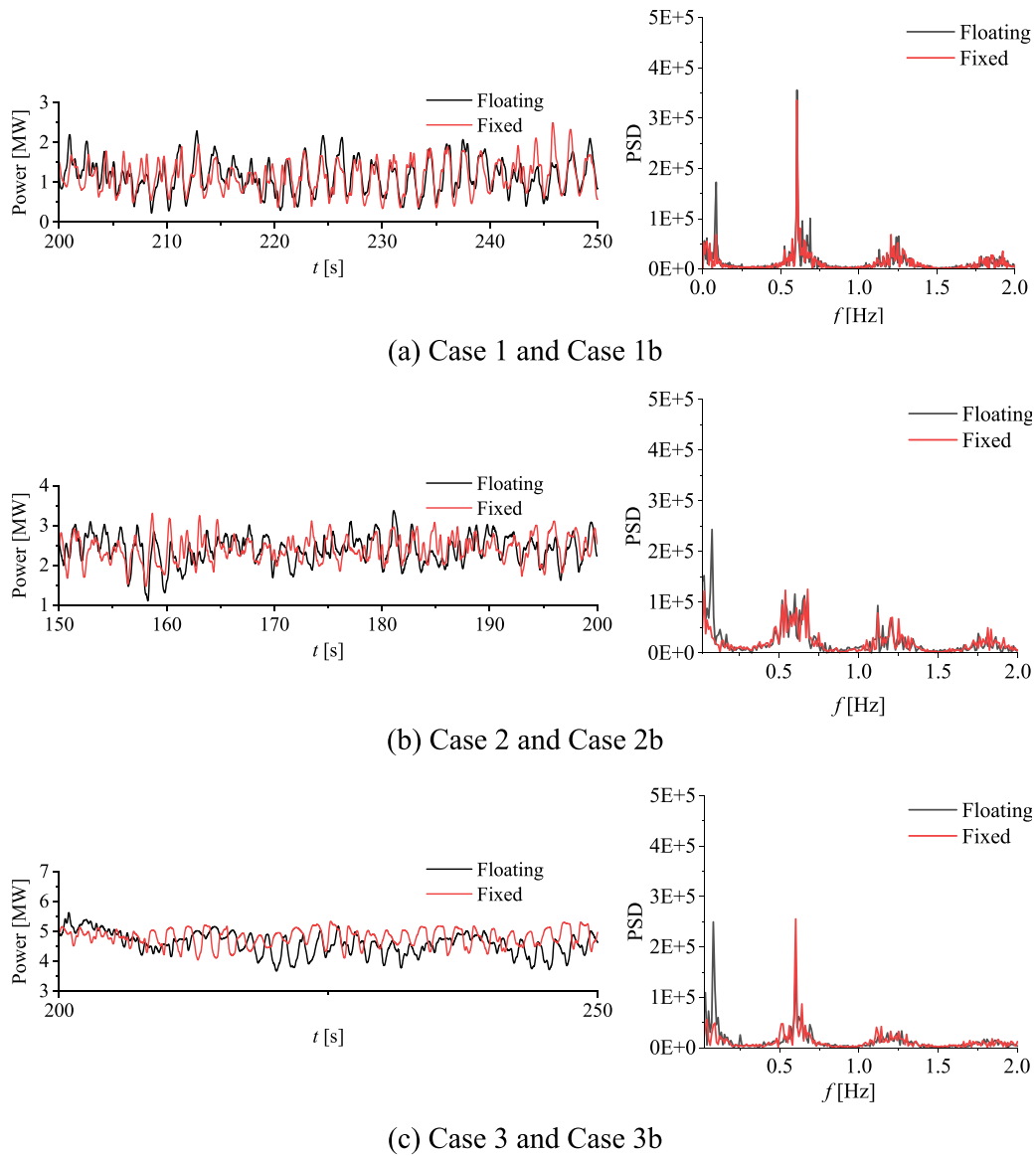


FIG. 16. Time series and FFT analysis of the power output of the third turbines.

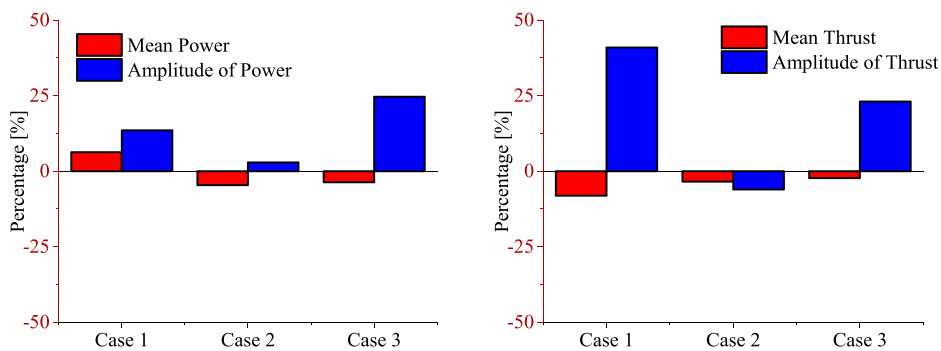


FIG. 17. Variation in aerodynamic parameters between fixed cases and FOWT cases, expressed as the percentage difference between the floating and fixed cases relative to the fixed cases.

03 March 2025 16:56:54

output, with a difference between them less than 6%. If the third turbine is fixed, the influence of the platform's motion is eliminated, and its power amplitude is generally smaller than the floating ones. The FOWT also shows a smaller thrust than the fixed one, which may be caused by the decreased relative wind velocity for turbines when the turbine moves, thus lowering the load components on the turbines.

### D. Staggered layouts

#### 1. Hydrodynamics of FOWTs

Staggered layouts from cases 4 to 6 are studied in this section. By setting the offset  $\Delta y_{12} = 1.5D$  between the first and second FOWT, it is expected that the second FOWT will not be affected by the wake of the first turbine, therefore, their power efficiency equals in these cases. By changing  $\Delta y_{13}$ , the power output and dynamic response of the third turbine are affected. In case 4 ( $\Delta y = 0$ ), the third turbine is only

affected by the wake of the first turbine, whereas in case 6 ( $\Delta y = 1.5D$ ), by the second turbine. Thus, to reduce the time cost, only two turbines are simulated for these two cases.

Figure 18 illustrates the dynamic response of each turbine. It shows that the surge amplitude increases with a larger  $\Delta y$  from cases 4 to 6, whereas the pitch amplitude decreases. The previous analysis in Fig. 9 indicates that pitch motion helps to reduce the power oscillations caused by surge motion. Therefore, the increase in surge amplitude coupled with the decrease in pitch amplitude resulted in higher motion amplitude at hub height. The time-averaged surge displayed in Fig. 18(c) is closely related to the power output and thrust, which reach their maximum in case 4, and the pitch angles decrease when  $\Delta y$  gets larger.

#### 2. Aerodynamics and wake interaction of FOWTs

Across three scenarios, the third turbine consistently produces less power than the upstream turbines. The maximum power output

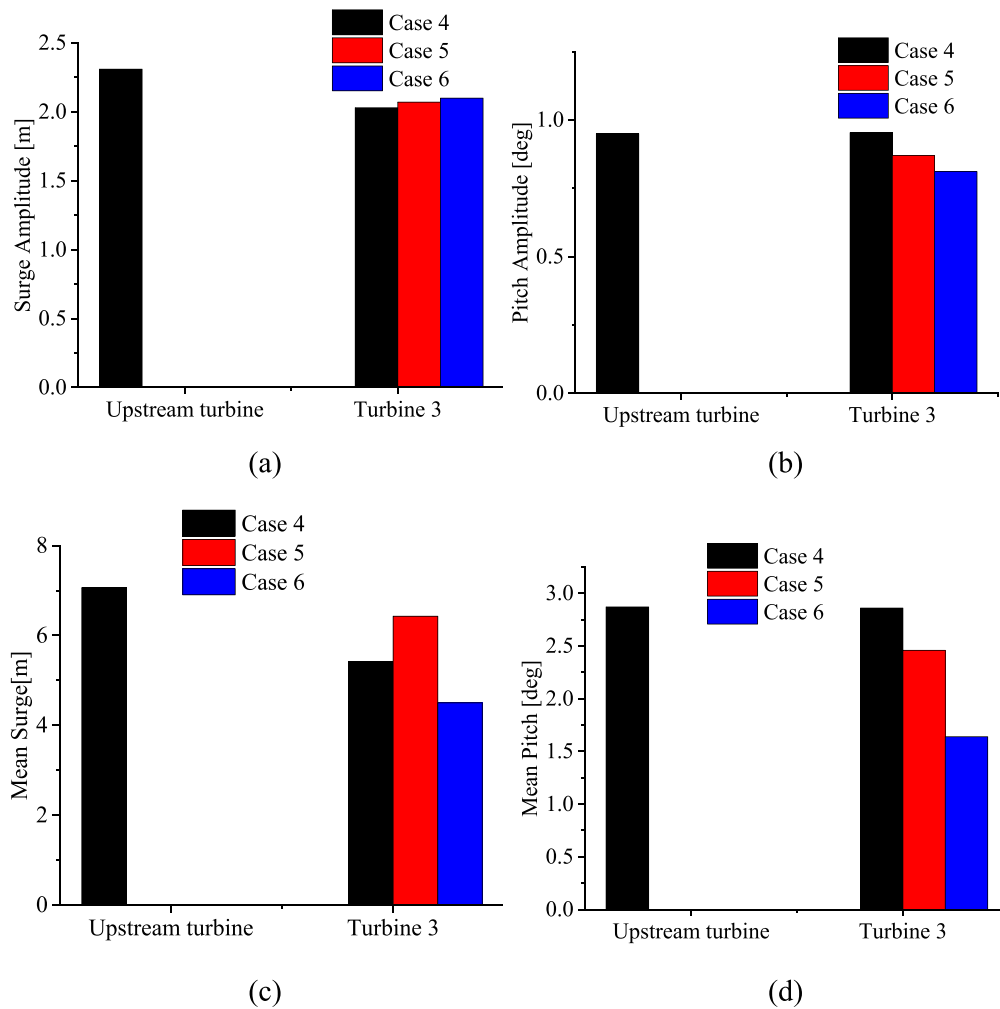


FIG. 18. (a) Surge and (b) pitch motion amplitude, time-averaged (c) surge, and (d) pitch of different FOWTs.

03 March 2025 16:56:54



of 4.2 MW occurs when the third turbine is positioned between the two upstream FOWTs in case 5. In case 4, the power output is 2.3 MW, which is higher than the 1.7 MW observed in case 6. This is because in case 4, the third turbine has a larger distance between the first turbine along the  $x$ -direction, thus benefiting from improved wake velocity recovery, resulting in an increased average power output. Compared to fixed turbines, the power output of FOWTs is marginally higher. In Fig. 19 the amplitude of power fluctuation is the largest for case 5, which is also the case for the thrust. Both amplitude and averaged thrust reach their maximum for case 5, where the third turbine is located in the middle of upstream turbines along the  $y$  direction.

From the velocity field in Fig. 20(b<sub>1</sub>), it can also be observed for case 5 that part of the inflow to the third turbine is between the wake area of the first two turbines and has a higher velocity region, which results in the highest power output among the three cases. Minimal interference between the wake loss regions of the first two turbines is evident, confirming that two turbine simulations for cases 4 and 6 are sufficient. By comparing Figs. 20(a<sub>2</sub>) and 20(c<sub>2</sub>), the wake from the upstream turbine gradually recovers its speed over a long propagation distance. Therefore, compared to case 6 with a shorter distance between the consecutive turbines, the power output in case 4 is greater. Additionally, in case 4, it is observed that the intensity of turbulence increases when propagating, while in case 6, it is lower due to short spacings. Thus, the aerodynamic performance is more influenced by platform motion than wind turbulence for case 6. This will be further discussed in Sec. IV D 3.

Figure 21 shows the visualization of the vortex structures. For cases 4 and 6, due to the different spacings from the upstream turbine, the inflow conditions vary for the third turbine. In case 4, the vortices generated at the blade roots progressively mix, leading to stronger turbulence around the rotor center compared to case 6. The components of wake turbulence also grow further than in case 4. Both lead to greater power fluctuation. In case 5, the third turbine is located between the two upstream turbines, a complete vortex structure is observable. The blade tips are influenced by the upstream vortices, which oppose the direction of those generated by the turbine itself, thus creating intense turbulent mixing and asymmetry downstream of the trailing edge. This phenomenon results in maximum energy at the blade passing frequency.

### 3. Platform motion contribution to aerodynamics performance

Figure 22 shows the time series of the third FOWT and the corresponding FFT analysis for different cases. In case 4, the frequencies corresponding to the blade passing frequency exhibit high energy density, particularly in the first and second-order components. These components have an energy density comparable to that of the wave frequency, which results from the platform's motion. In addition, in case 4, it is observed that the energy at the wave frequency for the floating scenario is only slightly higher than that in the fixed scenario. When increasing  $\Delta y$  from cases 4 to 6, the energy density at the wave frequency increases and becomes the dominant factor influencing power fluctuation in case 6.

The contribution of the platform's motion varies depending on specific cases, as shown in Fig. 23. It can be found more noticeable that the platform's motion is more influential in case 6 than in case 4. Combining the previous conclusion that turbulence increases with the distance between upstream and downstream turbines from the velocity profile in Fig. 20, the main factor affecting power output becomes the turbulence rather than the platform's motion, as in case 4. The average thrust in floating scenarios is nearly the same as in fixed ones, although the thrust amplitude in floating scenarios is greater than in fixed ones, which is induced by the platform's motion.

### E. Discussion

From Secs. IV C and IV D, it can be observed that gridded and staggered layouts exhibit different overall performance. By calculating the wind farm efficiency  $P_{total}/NP_{single}$ , where  $P_{total}$  is the total actual power output of the array,  $N$  is the number of turbines,  $P_{single}$  is the power of a single turbine without wake effects. Significant differences in efficiency between the two layouts can be identified. As shown in Fig. 24, the average power output of staggered layouts is generally higher than that of gridded layouts. Under proper placement conditions (case 5), even when the spacing between upstream and downstream turbines is only 3D, the overall power can still reach 92%, which is crucial for improving spatial utilization efficiency.

While the present study focuses on uniform inflow conditions to isolate and analyze the fundamental mechanisms, the realistic wind

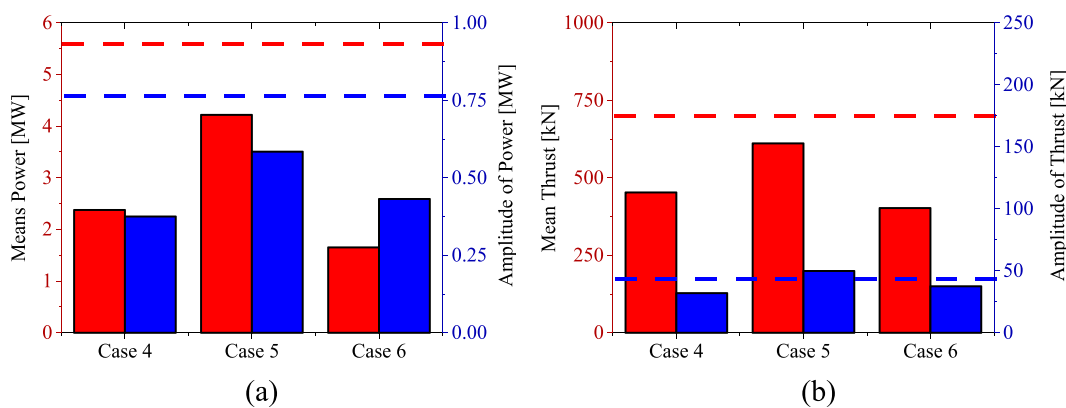
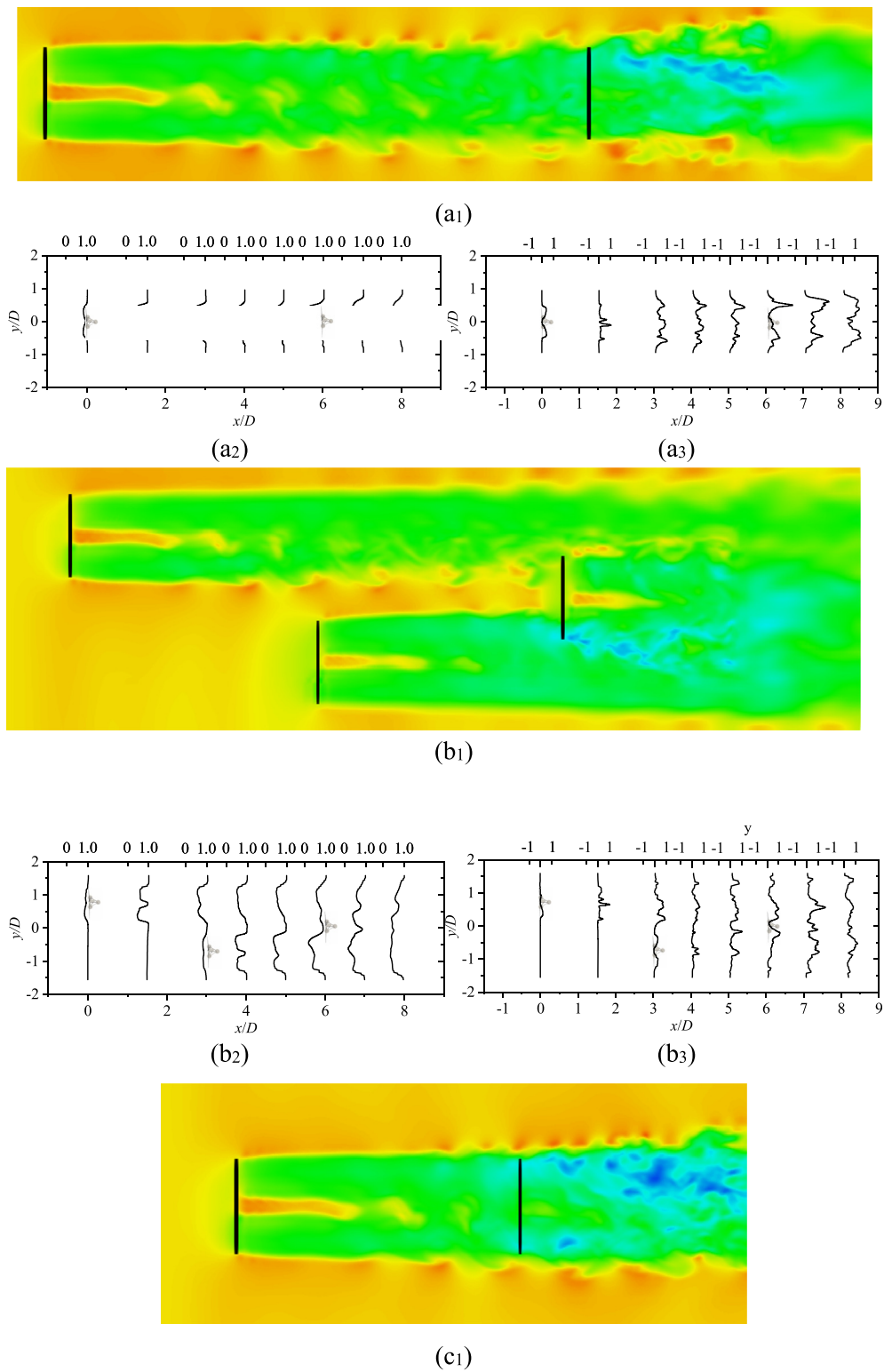


FIG. 19. (a) Time-averaged power output and amplitude of the power output. (b) Time-averaged thrust and amplitude of the thrust of the third turbine. The dashed lines denote the physical quantities of the first FOWT, while the dotted lines denote the physical quantities of the second FOWT.



**FIG. 20.** (a<sub>1</sub>–c<sub>1</sub>) Contours of spanwise velocity at hub height for at  $t = 200$  s; (a<sub>2</sub>–c<sub>2</sub>) the time-averaged velocity profile  $\bar{u}/U$  at different cross sections in the horizontal plane at hub height. (a<sub>3</sub>–c<sub>3</sub>) The corresponding time-averaged turbulence intensity profile. The subscripts denote the case number.

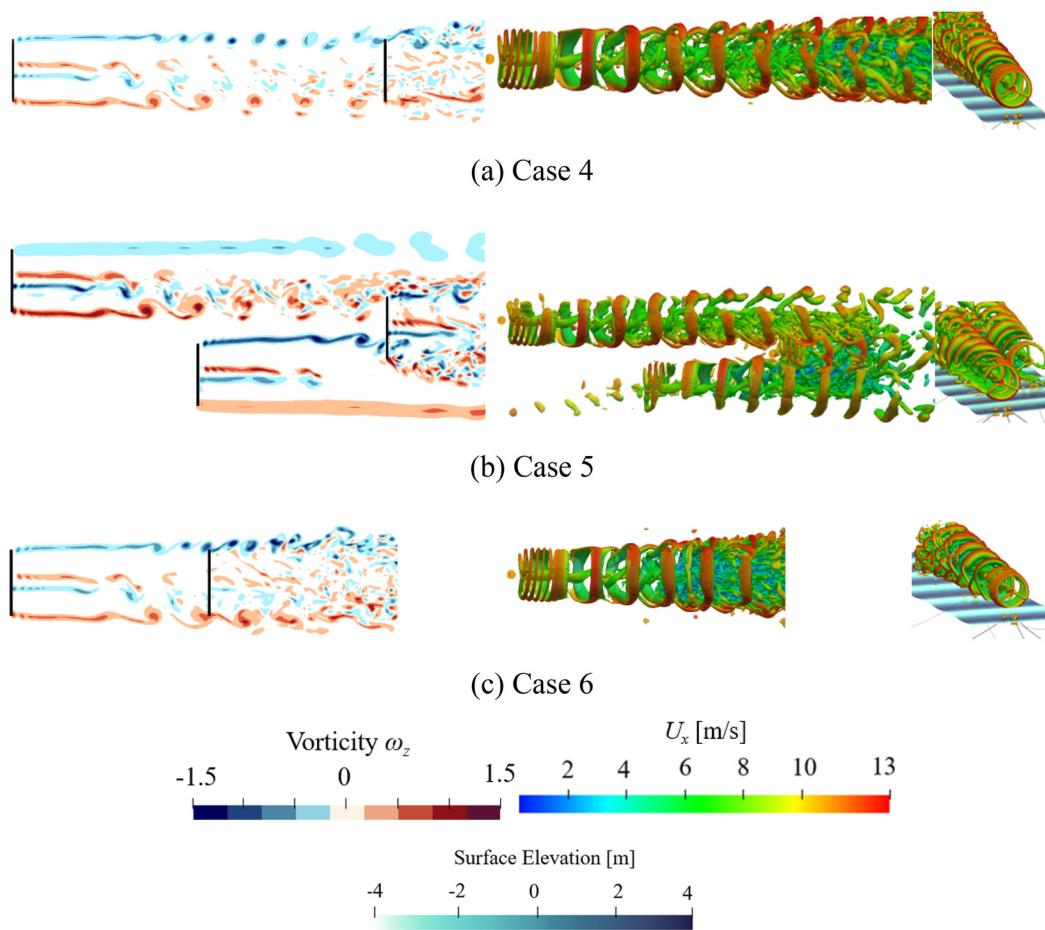
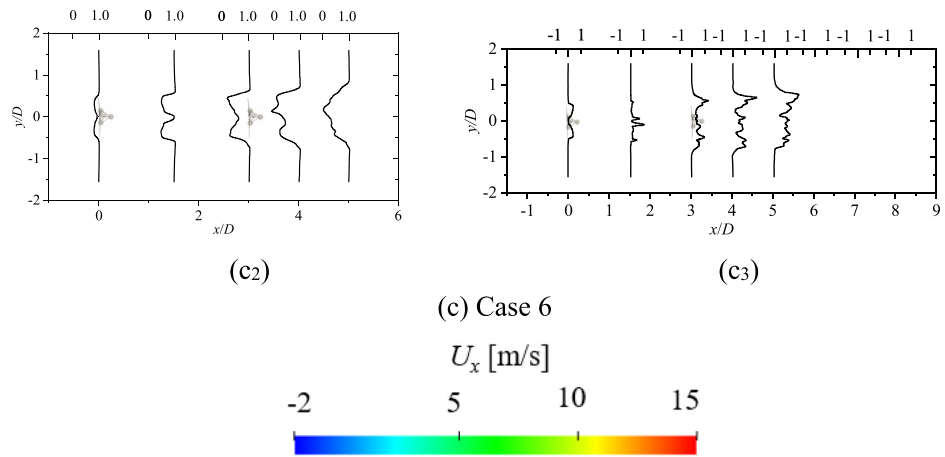
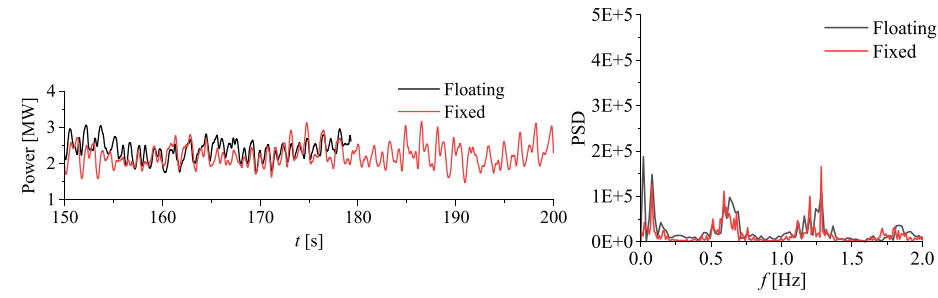
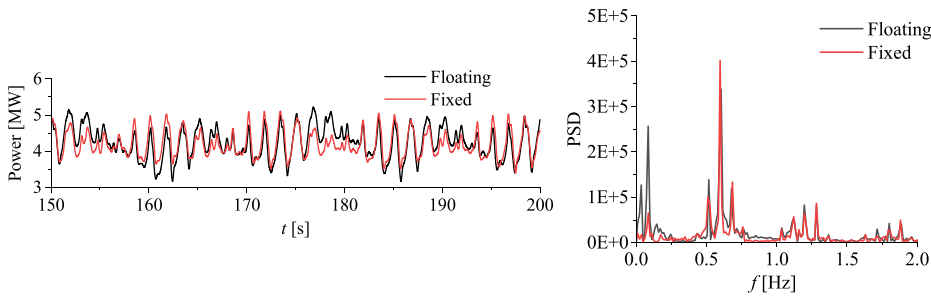


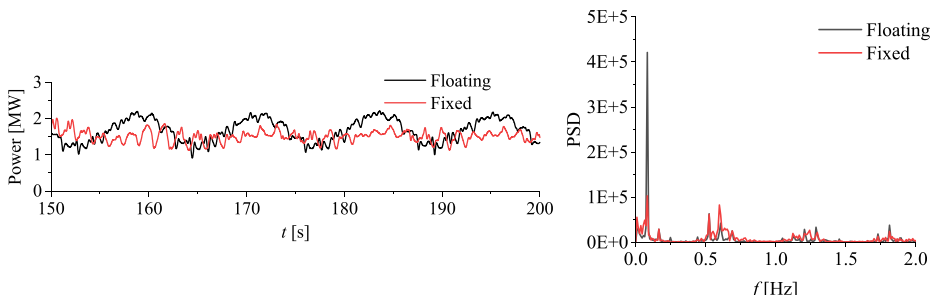
FIG. 21. Contours of spanwise vorticity at hub height and the vortex evolution (top and side view) represented by iso-surface of  $q = 0.002$  at  $t = 200$  s of each case. The surface elevation is also presented.



(a) Case 4 and Case 4b



(b) Case 5 and Case 5b



(c) Case 6 and Case 6b

FIG. 22. Time series and FFT analysis of the power output of the third turbines.

features may significantly influence wake breakdown and coherence. For example, changes in wind direction can alter the affected area of the wake region, making wake interference more complex. This is especially true for the compact turbine layout discussed in this study,

as it may cause downstream turbines to be influenced by the wakes of more upstream turbines. In addition, changes in wind speed can modify the vortex structure of the turbine wake, which in turn affects the relative contribution of platform motion. According to the results of

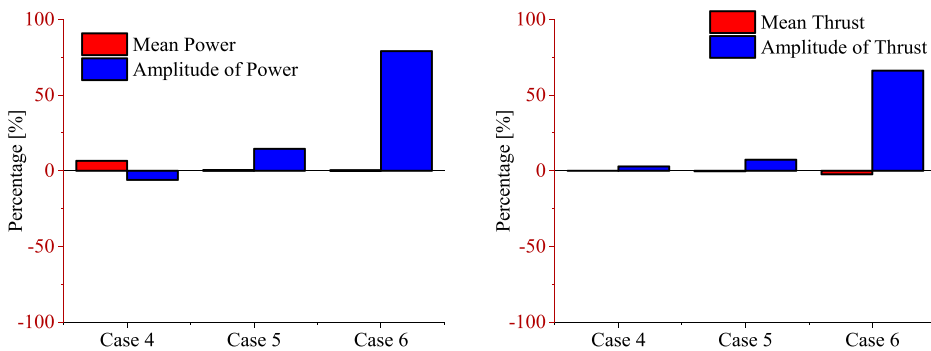


FIG. 23. Variation in aerodynamic parameters between fixed cases and FOWT cases, expressed as a percentage of the differences observed in the FOWT cases.

03 March 2025 16:56:54

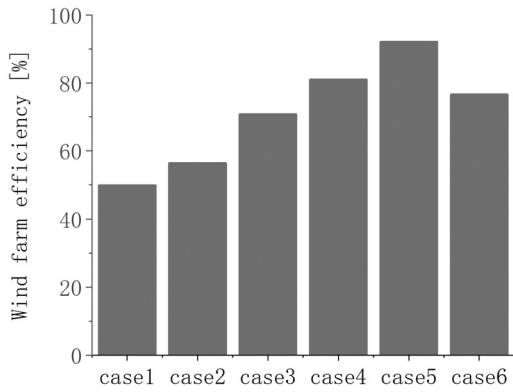


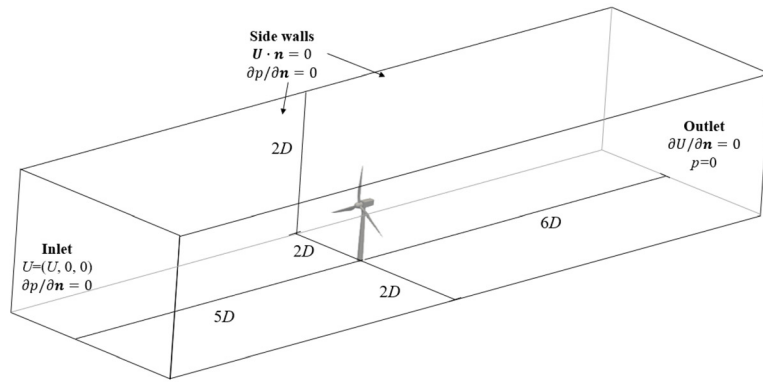
FIG. 24. Wind energy efficiency for different layouts.

this study, turbulence intensity and wind speed fluctuations have a significant impact on the performance of floating wind turbines. It can be anticipated that with the introduction of wind speed fluctuations and turbulence intensity, wake interference will become more pronounced, while the influence of platform motion on turbine output will be further reduced. In future work, we plan to extend the study to include turbulent inflow conditions to better capture the complexity of realistic operating environments and evaluate how motion response affects the observed wake characteristics and power production.

For FOWT farms, other advancing cost-efficiency and performance requires system-level innovations in the future. Promising directions include: (1) AI-optimized dynamic turbine layouts to minimize wake interactions while compensating for platform motions; (2) cooperative control strategies across turbines to balance energy capture and structural load mitigation; (3) modular floating structures with shared mooring systems, utilizing lightweight materials to reduce fabri-



(a)



(b)

FIG. 25. Sketch of the single turbine model in the (a) experiment and (b) computational domain with specific dimensions and boundary conditions.

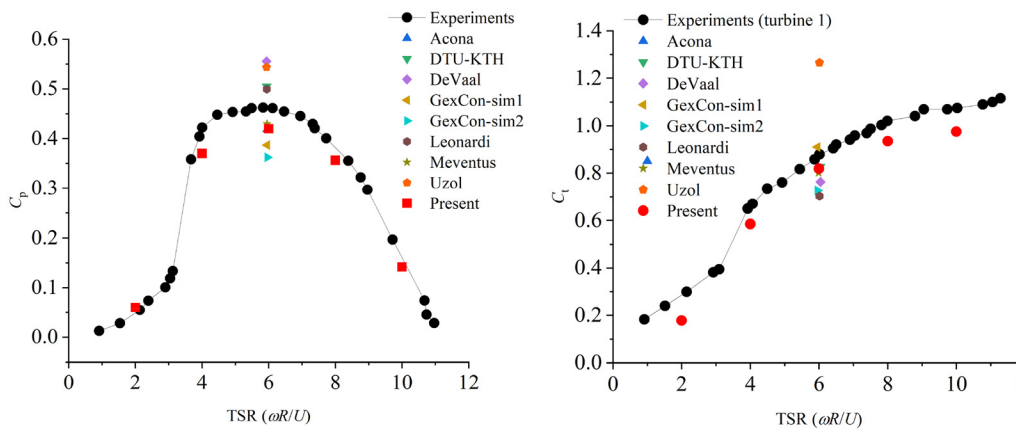
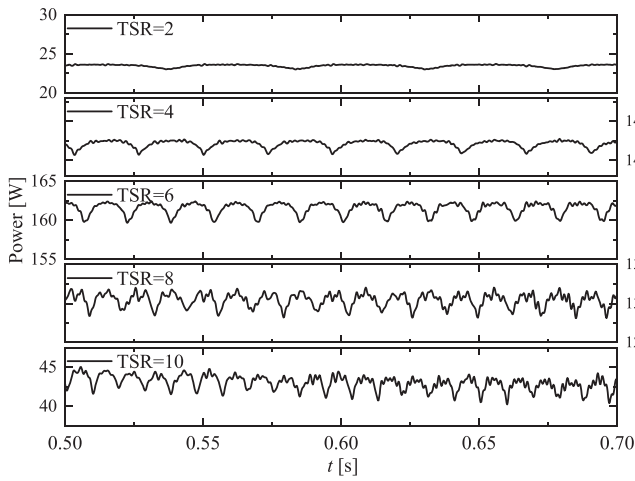
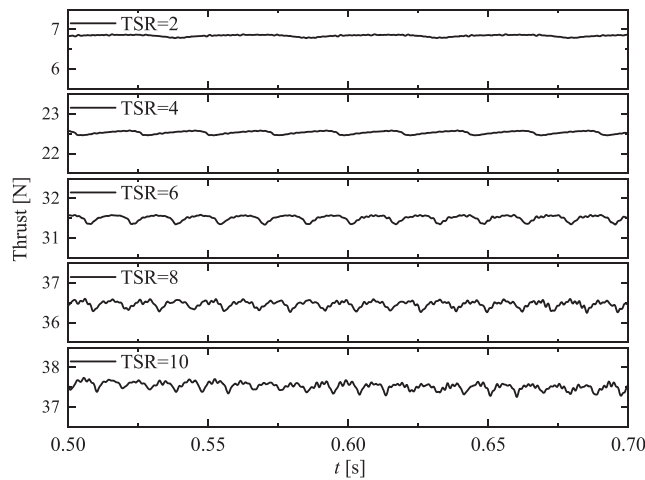


FIG. 26. Power and thrust coefficients  $C_p$  and  $C_t$  of the single turbine vs experimental data (Krogstad and Eriksen, 2013).



(a)



(b)

FIG. 27. Time series of (a) power output and (b) thrust with different TSRs.

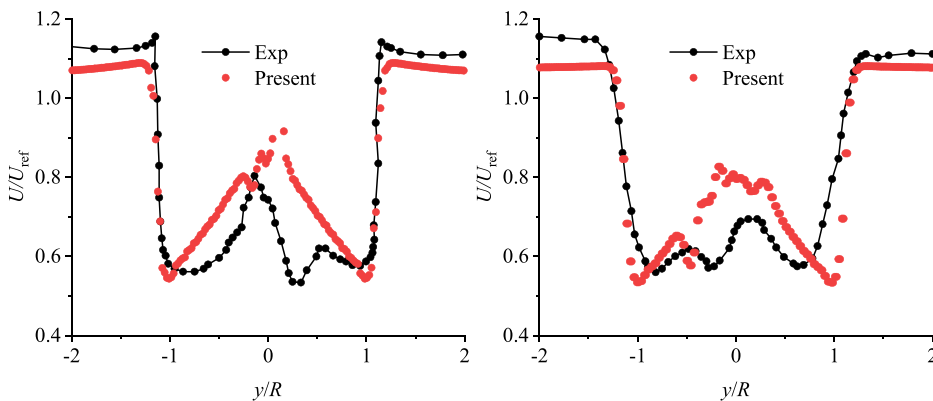


FIG. 28. Mean velocity profiles along the horizontal line with  $TSR = 6$  at a distance of (a)  $1D$  and (b)  $3D$  along the downstream direction.

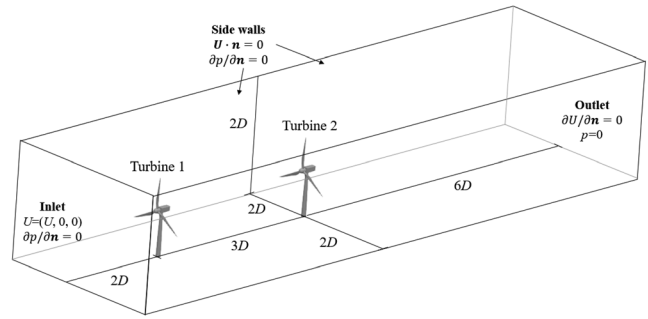


FIG. 29. Dimensions and boundary conditions for the computational domain of tandem fixed turbines.

ation/installation expenses; and (4) hybrid energy integration (e.g., combining wind, wave, and solar) to maximize infrastructure sharing and grid resilience. These integrated approaches target the complex interdependencies between turbines, environmental dynamics, and scalability barriers, ultimately driving down LCOE while enhancing power output and operational robustness.

### V. CONCLUSION

This paper studies wave interaction with multiple FOWTs with different layouts in which a significant wake interaction exists. To save the computational time cost by avoiding the meshing of the blades, the ALM is coupled with the present tool to solve the aerodynamics. The hydrodynamics are solved simultaneously with aerodynamics in the same computational domain.

In comparison, the average power output of staggered layouts is typically greater than that of gridded layouts. For gridded layouts, the power output of the third turbine is significantly reduced due to wind speed loss. This loss decreases as the  $y$  position increases. For staggered layouts, when the third turbine is positioned between two upstream turbines, its power is less affected by upstream wakes, and the wind farm efficiency of the whole array can reach 92%. Therefore, staggered arrangements allow for more turbines to be accommodated in a limited space while still achieving substantial power outputs.

The comparison also reveals that whether the third turbine is fixed or not has a limited impact on its average power. However, the motion of the turbines significantly affects the amplitude of power

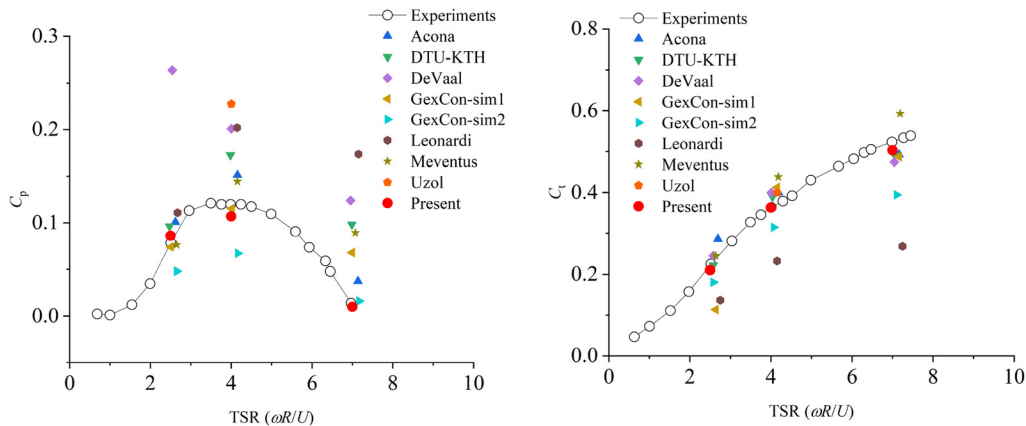


FIG. 30. Power and thrust coefficients  $C_p$  and  $C_t$  for  $T_2$  against experimental data.

fluctuations. In the case of gridded layouts, the fluctuation amplitude of the mobile turbines can be up to 25% higher than that of the fixed turbines. For staggered layouts, this figure can reach 80%.

Spectral analysis also shows that in case 1 of gridded layout, the impact of platform motion on power fluctuations diminishes from upstream to downstream while the influence of wind turbulence increases. This implies that under more turbulent wind conditions, the influence of the platform’s motion on power generation is reduced.

**AUTHOR DECLARATIONS**

**Conflict of Interest**

The authors have no conflicts to disclose.

**Author Contributions**

**Xiang Li:** Conceptualization (equal); Data curation (equal); Formal analysis (equal); Funding acquisition (equal); Investigation (equal); Methodology (equal); Project administration (equal); Resources (equal); Software (equal); Supervision (equal); Validation (equal); Visualization (equal); Writing – original draft (equal); Writing – review & editing (equal). **Qing Xiao:** Conceptualization (equal); Investigation (equal); Methodology (equal); Resources (equal); Supervision (equal); Writing – original draft (equal); Writing – review & editing (equal). **Yang Huang:** Conceptualization (equal); Methodology (equal); Software (equal); Writing – review & editing (equal).

**DATA AVAILABILITY**

The data that supports the findings of this study are available within the article.

**APPENDIX A: VALIDATION OF SINGLE FIXED TURBINE**

CFD results of the single fixed turbine are validated against the “Blind test” data on wind turbine wake modeling organized jointly by Nowitech and Norcowe in Bergen in October 2011, as shown in Fig. 25(a). The turbine model is designed to be simple, and the same airfoil NREL S826, 14% thick, was used throughout the span. The

blades were made of aluminum, and the maximum load on each blade was estimated to be about 15 N. The turbine model was characterized by a rotor diameter of  $D = 0.894$  m, with wind speeds subjected to it at  $U_\infty = 10$  m/s. The height of the rotor is 0.817 m. Furthermore, its rated Tip Speed Ratio (TSR, representing the ratio between the wind speed and the speed of the tips of the wind turbine) was set at  $\lambda = 6.0$ . For more details about the turbine, readers can refer to the reference. This study explores five distinct cases, each

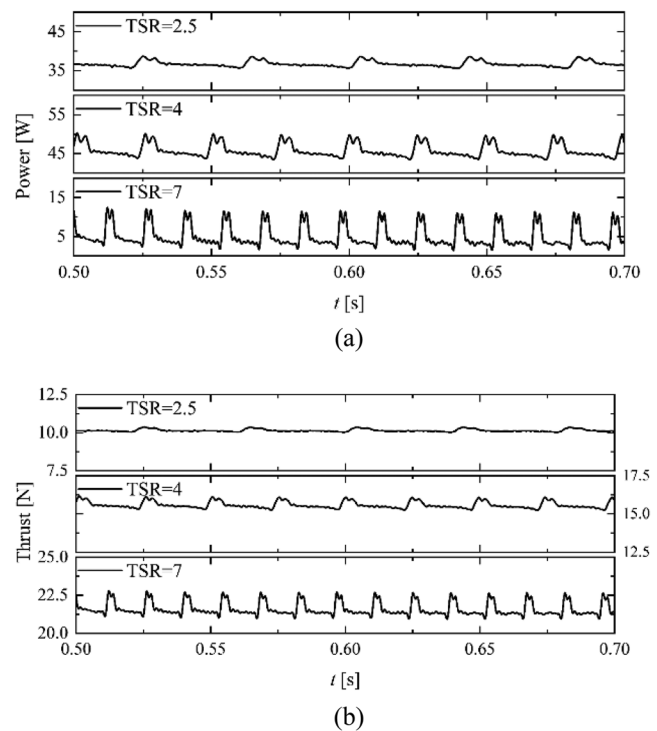


FIG. 31. Time series of power output and thrust of the downstream turbine with different TSRs.

marked by  $\lambda = 2, 4, 6, 8,$  and  $10,$  which is achieved by altering the rotor's speed. The sketch of the numerical wind tunnel is shown in Fig. 25(b). The dimension of the computational domain is  $11D \times 4D \times 2D.$  The turbine is  $5D$  from the inlet and  $6D$  from the outlet boundary. The boundary conditions are also annotated in Fig. 25(b). A constant wind velocity  $U_\infty$  along the  $x$  axis is applied on the inlet boundary, while a constant pressure outlet  $p = 0$  is defined. A symmetry boundary condition is used for the other four side walls. The length of the background cell is  $0.063$  m, while the length of the cell near the turbine and wake zone is  $25\%$  of the background cell length. The total cell count is  $5.15 \times 10^6$  for the whole domain.

Figure 26 provides the power and thrust coefficients  $C_p$  and  $C_t,$  which are defined by

$$C_p = \frac{P}{0.5\rho S v^3} \quad \text{and} \quad C_t = \frac{P}{0.5\rho_{air} S U^2} \quad (A1)$$

where  $P$  is the power output, and  $S$  is the swept area of the turbine blades. The results are validated against experimental data and other numerical results. The left graph depicting power coefficient

$C_p$  reveals a bell-curve trend for the experimental data, with the peak power coefficient observed around  $\lambda = 6.$  Among the various simulation methods, the present data closely aligns with the experimental results within a wider TSR range from 2 to 10. The thrust coefficient  $C_t$  shows an increasing trend in the experiment. Again, the present simulation data aligns closely with this trend, underscoring its accuracy.

In Fig. 27, the power output and thrust variation with time can be seen. The fluctuations can be found, whose periods increase with the TSR. The fluctuation frequency matches thrice the rotor's frequency, equating to the blade-passing frequency, given the turbine has three blades. This pattern could come from varying wind conditions encountered by each blade during rotation. As the blades move, they experience shifts in wind velocity and angle, leading to a cyclical variation in power generation. Although the amplitude of the fluctuations increases with TSR, it can be neglected compared to their time-averaged value.

The wake velocity of the single turbine is also compared in Fig. 28. The velocity along a horizontal line at the hub height is

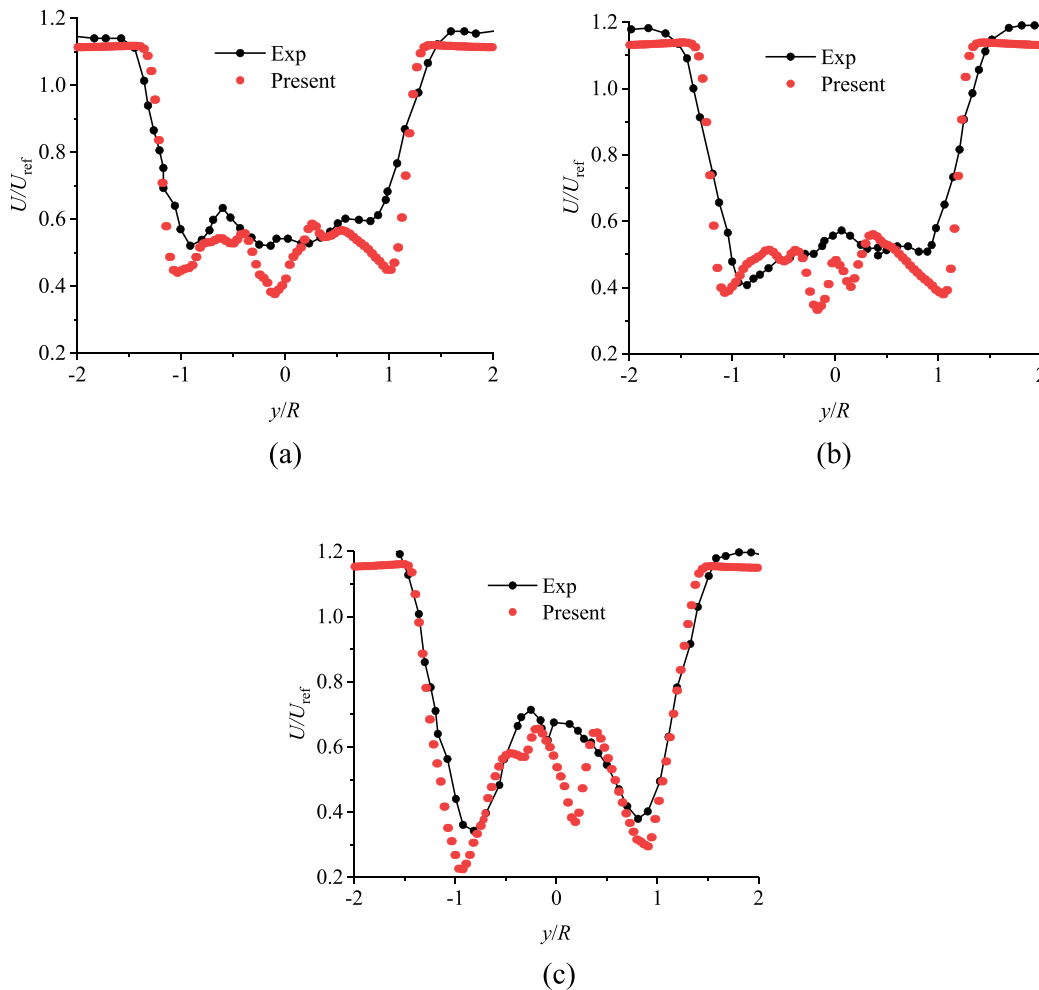


FIG. 32. Mean velocity profiles along the horizontal line at a distance of  $1D$  of the downstream turbine with TSR of (a) 2.5, (b) 4.0, and (c) 7.0.



sampled; each of them is time-averaged and normalized by the incident wind speed  $U_\infty = 10$  m/s. The position is normalized by the rotor's radius  $D$ . It can be seen the present study aligns well with experimental measurements, evidencing a strong correlation in wake behavior. Despite some discrepancies, the pronounced central velocity deficit and its attenuation downstream are captured accurately.

## APPENDIX B: VALIDATION OF TANDEM FIXED TURBINES

This section is to validate the accuracy regarding performance changes caused by the wake interference between turbines. A second turbine is deployed downstream the upstream turbine discussed in Sec. III. It has a slightly larger rotor diameter of 0.944 m and a rated TSR of 4.0. The distance between the two turbines is  $3D$ . Since ALM does not need meshing the turbine geometry in the computational domain, the mesh for single turbine validation is re-used. For this setup, three distinct cases were examined:

Case A, where the TSR for the downstream turbine is set at the standard value of 4; case B, an optional high-speed scenario with the downstream turbine at a TSR of 7; case C, an optional low-speed case where the downstream turbine has a TSR of 2.5. To better understand the setup, the layout of the two turbines is shown in Fig. 29. In Fig. 30,  $C_p$  and  $C_t$  for the downstream turbine are compared against the experimental data across a range of TSRs. The present results consistently follow the experimental trend, especially in the crucial mid-range TSR values. It can be seen that the performance of the downstream turbines is weakened due to the low-velocity wake region created by the upstream turbines with high-turbulence, leading to a significant drop in power output. A peak in the power coefficient can be observed near a TSR of 4, and it is seen that the current model closely reflects these experimental values.

In Fig. 31, the time series of power output and thrust are displayed for three distinct TSRs. The stability and periodic behavior of both coefficients over time provide insights into the system's dynamic response. Both power and thrust coefficients demonstrate stable oscillations, suggesting a consistent turbine response over time for each TSR circle. The wake velocity profile shown in Fig. 32 also shows good agreement for different TSRs. In summary, the presented data for tandem fixed turbines indicates that the current modeling approach not only aligns closely with experimental results but also provides stable and consistent outputs across various TSR values, reinforcing the model's robustness and reliability.

## REFERENCES

- L. A. H. Machielse, P. J. Eecen, H. Korterink, S. P. van der Pijl, and J. G. Schepers, *ECN Test Farm Measurements for Validation of Wake Models* (ECN, Petten, 2007).
- E. Migoya, A. Crespo, J. Garcia, F. Moreno, F. Manuel, A. Jimenez, and A. Costa, "Comparative study of the behavior of wind-turbines in a wind farm," *Energy* **32**, 1871 (2007).
- D. Cabezón Martínez, K. S. Hansen, and R. J. Barthelmie, "Analysis and validation of CFD wind farm models in complex terrain. Effects induced by topography and wind turbines," European Wind Energy Conference & Exhibition (EWEC 2010) (2010).
- A. P. Hendradewa and S. Yin, "Comparative analysis of offshore wind turbine blade maintenance: RL-based and classical strategies for sustainable approach," *Rel. Eng. Syst. Safety* **253**, 110477 (2025).
- S. Mujibur Rahman, H. Chattopadhyay, and P. Dutta, "Computational fluid dynamics analysis on performance assessment of Darrieus-type vertical axis wind turbine using NACA0016, NACA0019 and NACA0020 airfoil sections," *Int. J. Ambient Energy* **45**, 2315489 (2024).
- L. Yang, B. Li, Y. Dong, Z. Hu, K. Zhang, and S. Li, "Large-amplitude rotation of floating offshore wind turbines: A comprehensive review of causes, consequences, and solutions," *Renewable Sustainable Energy Rev.* **211**, 115295 (2025).
- T. Tran, D. Kim, and J. Song, "Computational fluid dynamic analysis of a floating offshore wind turbine experiencing platform pitching motion," *Energies* **7**, 5011 (2014).
- T. T. Tran and D.-H. Kim, "A CFD study into the influence of unsteady aerodynamic interference on wind turbine surge motion," *Renewable Energy* **90**, 204 (2016).
- S. Xu, T. Zhuang, W. Zhao, and D. Wan, "Numerical investigation of aerodynamic responses and wake characteristics of a floating offshore wind turbine under atmospheric boundary layer inflows," *Ocean Eng.* **279**, 114527 (2023).
- V. Leble and G. Barakos, "10-MW wind turbine performance under pitching and yawing motion," *J. Sol. Energy Eng.* **139**, 041003 (2017).
- Y. Liu, Q. Xiao, A. Incecik, C. Peyrard, and D. Wan, "Establishing a fully coupled CFD analysis tool for floating offshore wind turbines," *Renewable Energy* **112**, 280 (2017).
- A. Rezaeiha and D. Micallef, "Wake interactions of two tandem floating offshore wind turbines: CFD analysis using actuator disc model," *Renewable Energy* **179**, 859 (2021).
- A. Arabgolarcheh, S. Jannesarahmadi, and E. Benini, "Modeling of near wake characteristics in floating offshore wind turbines using an actuator line method," *Renewable Energy* **185**, 871 (2022).
- A. Arabgolarcheh, A. Rouhollahi, and E. Benini, "Analysis of middle-to-far wake behind floating offshore wind turbines in the presence of multiple platform motions," *Renewable Energy* **208**, 546 (2023).
- A. Arabgolarcheh, D. Micallef, A. Rezaeiha, and E. Benini, "Modelling of two tandem floating offshore wind turbines using an actuator line model," *Renewable Energy* **216**, 119067 (2023).
- P. Fleming, P. M. O. Gebraad, S. Lee, J.-W. van Wingerden, K. Johnson, M. Churchfield, J. Michalakes, P. Spalart, and P. Moriarty, "Simulation comparison of wake mitigation control strategies for a two-turbine case," *Wind Energy* **18**, 2135 (2015).
- F. González-Longatt, P. Wall, and V. Terzija, "Wake effect in wind farm performance: Steady-state and dynamic behavior," *Renewable Energy* **39**, 329 (2012).
- G.-W. Qian and T. Ishihara, "Wind farm power maximization through wake steering with a new multiple wake model for prediction of turbulence intensity," *Energy* **220**, 119680 (2021).
- J. W. Wagenaar, L. Machielse, and J. Schepers, "Controlling wind in ECN's scaled wind farm," Europe Premier Wind Energy Event (2012).
- Á. Jiménez, A. Crespo, and E. Migoya, "Application of a LES technique to characterize the wake deflection of a wind turbine in yaw," *Wind Energy* **13**, 559 (2010).
- A. C. Kheirabadi and R. Nagamune, "A quantitative review of wind farm control with the objective of wind farm power maximization," *J. Wind Eng. Ind. Aerodyn.* **192**, 45 (2019).
- X. Li, C. Zhu, Z. Fan, X. Chen, and J. Tan, "Effects of the yaw error and the wind-wave misalignment on the dynamic characteristics of the floating offshore wind turbine," *Ocean Eng.* **199**, 106960 (2020).
- S. N. Rodriguez and J. W. Jaworski, "Strongly-coupled aeroelastic free-vortex wake framework for floating offshore wind turbine rotors. Part 2: Application," *Renewable Energy* **149**, 1018 (2020).
- X. Shen, J. Chen, P. Hu, X. Zhu, and Z. Du, "Study of the unsteady aerodynamics of floating wind turbines," *Energy* **145**, 793 (2018).
- Y. Huang, W. Zhao, and D. Wan, "Wake interaction between two spar-type floating offshore wind turbines under different layouts," *Phys. Fluids* **35**, 097102 (2023).
- A. C. Kheirabadi and R. Nagamune, "A low-fidelity dynamic wind farm model for simulating time-varying wind conditions and floating platform motion," *Ocean Eng.* **234**, 109313 (2021).

- <sup>27</sup>H. Jasak, A. Jemcov, and Z. Tukovic, *OpenFOAM: A C++ Library for Complex Physics Simulations* (IUC, Dubrovnik, Croatia, 2007).
- <sup>28</sup>C. W. Hirt and B. D. Nichols, "Volume of fluid (VOF) method for the dynamics of free boundaries," *J. Comput. Phys.* **39**, 201 (1981).
- <sup>29</sup>P. Higuera, "Enhancing active wave absorption in RANS models," *Appl. Ocean Res.* **94**, 102000 (2020).
- <sup>30</sup>N. Trolborg, J. N. Sorensen, and R. Mikkelsen, "Numerical simulations of wake characteristics of a wind turbine in uniform inflow," *Wind Energy* **13**, 86 (2010).
- <sup>31</sup>X. Li, Q. Xiao, E. Wang, C. Peyrard, and R. T. Gonçalves, "The dynamic response of floating offshore wind turbine platform in wave-current condition," *Phys. Fluids* **35**, 087113 (2023).
- <sup>32</sup>R. Shakoor, M. Y. Hassan, A. Raheem, and Y.-K. Wu, "Wake effect modeling: A review of wind farm layout optimization using Jensen's model," *Renewable Sustainable Energy Rev.* **58**, 1048 (2016).
- <sup>33</sup>C. Han and R. Nagamune, *Position Control of an Offshore Wind Turbine with a Semi-Submersible Floating Platform Using the Aerodynamic Force* (IEEE, 2016).
- <sup>34</sup>Z. Fan, S. Li, Z. Gao, L. Zhang, X. Zheng, W. Zhu, W. Shen, M. Sjöholm, T. K. Mikkelsen, and T. Wang, "On the importance of wind turbine wake boundary to wind energy and environmental impact," *Energy Convers. Manage.* **277**, 116664 (2023).
- <sup>35</sup>A. C. Kheirabadi and R. Nagamune, "Real-time relocation of floating offshore wind turbine platforms for wind farm efficiency maximization: An assessment of feasibility and steady-state potential," *Ocean Eng.* **208**, 107445 (2020).
- <sup>36</sup>G. Froese, S. Y. Ku, A. C. Kheirabadi, and R. Nagamune, "Optimal layout design of floating offshore wind farms," *Renewable Energy* **190**, 94 (2022).
- <sup>37</sup>A. C. Kheirabadi and R. Nagamune, *Modeling and Power Optimization of Floating Offshore Wind Farms with Yaw and Induction-based Turbine Repositioning* (IEEE, 2019).
- <sup>38</sup>A. Arabgolarcheh, D. Micallef, and E. Benini, "The impact of platform motion phase differences on the power and load performance of tandem floating offshore wind turbines," *Energy* **284**, 129271 (2023).
- <sup>39</sup>See <http://www.cirrus.ac.uk> for information about EPCC's Advanced Computing Facility.
- <sup>40</sup>Y. Huang, Y. Zhuang, and D. Wan, "Hydrodynamic study and performance analysis of the OC4-DeepCwind platform by CFD method," *Int. J. Comput. Methods* **18**, 2050020 (2021).